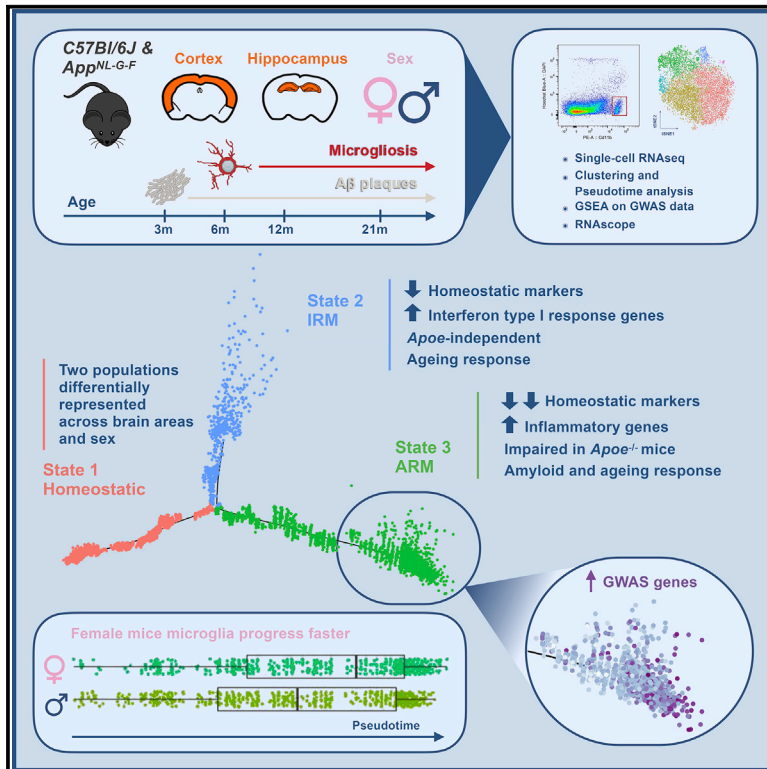# The Major Risk Factors for Alzheimer's Disease: Age, Sex, and Genes Modulate the Microglia Response to Aβ Plaques

Graphical Abstract

Authors

Carlo Sala Frigerio, Leen Wolfs, Nicola Fattorelli, ..., V. Hugh Perry, Mark Fiers, Bart De Strooper

Correspondence

carlo.salafrigerio@kuleuven.vib.be (C.S.F.),
bart.destrooper@kuleuven.vib.be (B.D.S.)

In Brief

Sala Frigerio et al. show how microglia respond to amyloid-β, the Alzheimer's disease (AD)-causing factor. Their major response, the ARMs response, is enriched for AD risk genes, is abolished by *Apoe* deletion, develops faster in female mice, and is also part of normal aging. Thus, major AD risk factors converge on microglia.

Highlights

- Exposure to Aβ in AD potentiates a microglia response present during normal aging

- This microglia response is heterogeneous with potential synaptotoxic subtypes

- Microglia in female mice develop this response faster than in male mice

- *Apoe* deletion blocks the main response of microglia to Aβ

CellPress

The Major Risk Factors for Alzheimer's Disease: Age, Sex, and Genes Modulate the Microglia Response to Aβ Plaques

Carlo Sala Frigerio,[1,2,3,*] Leen Wolfs,[1,2] Nicola Fattorelli,[1,2] Nicola Thrupp,[1,2] Iryna Voytyuk,[1,2] Inga Schmidt,[1,2] Renzo Mancuso,[1,2] Wei-Ting Chen,[1,2] Maya E. Woodbury,[4] Gyan Srivastava,[4] Thomas Möller,[4] Eloise Hudry,[5] Sudeshna Das,[5] Takaomi Saido,[6] Eric Karran,[4] Bradley Hyman,[5] V. Hugh Perry,[3,7] Mark Fiers,[1,2] and Bart De Strooper[1,2,3,8,*]

[1]VIB Centre for Brain Disease Research, Leuven, Belgium
[2]University of Leuven, Department of Neurosciences and Leuven Brain Institute, Leuven, Belgium
[3]UK Dementia Research Institute, University College London, London, UK
[4]Foundational Neuroscience Center, AbbVie, Inc., Cambridge, MA, USA
[5]Department of Neurology, MassGeneral Institute for Neurodegenerative Disease, Massachusetts General Hospital, Harvard Medical School, Charlestown, MA, USA
[6]Laboratory for Proteolytic Neuroscience, RIKEN Brain Science Institute, Wako-shi, Saitama, Japan
[7]Centre for Biological Sciences, University of Southampton, Southampton, UK
[8]Lead Contact
*Correspondence: carlo.salafrigerio@kuleuven.vib.be (C.S.F.), bart.destrooper@kuleuven.vib.be (B.D.S.)
https://doi.org/10.1016/j.celrep.2019.03.099

SUMMARY

Gene expression profiles of more than 10,000 individual microglial cells isolated from cortex and hippocampus of male and female App^{NL-G-F} mice over time demonstrate that progressive amyloid-β accumulation accelerates two main activated microglia states that are also present during normal aging. Activated response microglia (ARMs) are composed of specialized subgroups overexpressing MHC type II and putative tissue repair genes (*Dkk2*, *Gpnmb*, and *Spp1*) and are strongly enriched with Alzheimer's disease (AD) risk genes. Microglia from female mice progress faster in this activation trajectory. Similar activated states are also found in a second AD model and in human brain. *Apoe*, the major genetic risk factor for AD, regulates the ARMs but not the interferon response microglia (IRMs). Thus, the ARMs response is the converging point for aging, sex, and genetic AD risk factors.

INTRODUCTION

Alzheimer's disease (AD) is characterized by typical biochemical lesions (β-amyloid peptide [Aβ] plaques and tau tangles) accompanied by extensive cellular changes (neuronal dystrophic alterations, neuronal cell loss, astrogliosis, and microgliosis) (De Strooper and Karran, 2016; Serrano-Pozo et al., 2011). Rare mutations in amyloid precursor protein (*APP*), presenilin (*PSEN*) 1 and 2 (Karch et al., 2014), *ADAM10* (Suh et al., 2013), and *ADAM17* (Hartl et al., 2018) trigger Aβ plaque accumulation and are sufficient to induce the full biochemical and morphological signature of AD. While this clearly indicates a major role for

Aβ in AD pathology (Jack et al., 2013; Selkoe and Hardy, 2016), even in these genetic forms, a decades-long asymptomatic phase is present (Bateman et al., 2012). Thus, in addition to Aβ plaques, other pathological processes, either in response to or in parallel to Aβ accumulation, need activation to cause neurodegenerative disease (De Strooper and Karran, 2016).

The search for the genetic risk determinants in sporadic AD has highlighted the central role of non-neuronal genes in pathways that do not appear directly related to Aβ metabolism (Cruchaga et al., 2014; Guerreiro et al., 2013; Lambert et al., 2013; Marioni et al., 2018; Salih et al., 2018; Sims et al., 2017; Villegas-Llerena et al., 2016). Most of the genes associated with the ~40 loci identified by genome-wide association (GWA) analysis or by rare variant sequencing studies are expressed in glial cells (e.g., *APOE*, *TREM2*, *BIN1*, *CD33*, *INPP5D*, *CTSB*, *CTSD*, and *PICALM*). Moreover, analysis of available single-cell transcriptome datasets for human brain cells reported an association between AD GWA signals and microglia as well as astrocytes (Calderon et al., 2017). Analysis of regulatory networks of genes differentially expressed in AD patients indicates that immune- and microglia-specific gene modules are key contributors to AD pathology (Zhang et al., 2013). Thus, genetic and molecular evidence suggest that Aβ accumulation is the trigger of a series of pathogenic processes in which microglia play a central role. No consistent hypothesis, however, links the causality implied by the mutations in the amyloid pathway genes to the genetic risk linking sporadic AD to inflammatory pathways. This has caused severe criticism on the amyloid cascade hypothesis for AD, raising questions about its validity in sporadic AD (Behl and Ziegler, 2017; Harrison and Owen, 2016; Herrup, 2015; Karran and Hardy, 2014; Makin, 2018; Selkoe and Hardy, 2016). One possible resolution is that amyloid pathology acts only as a trigger in sporadic AD (Karran et al., 2011); i.e., Aβ accumulation is necessary but insufficient to cause full-blown disease. The cellular response, determined by the genetic makeup of the
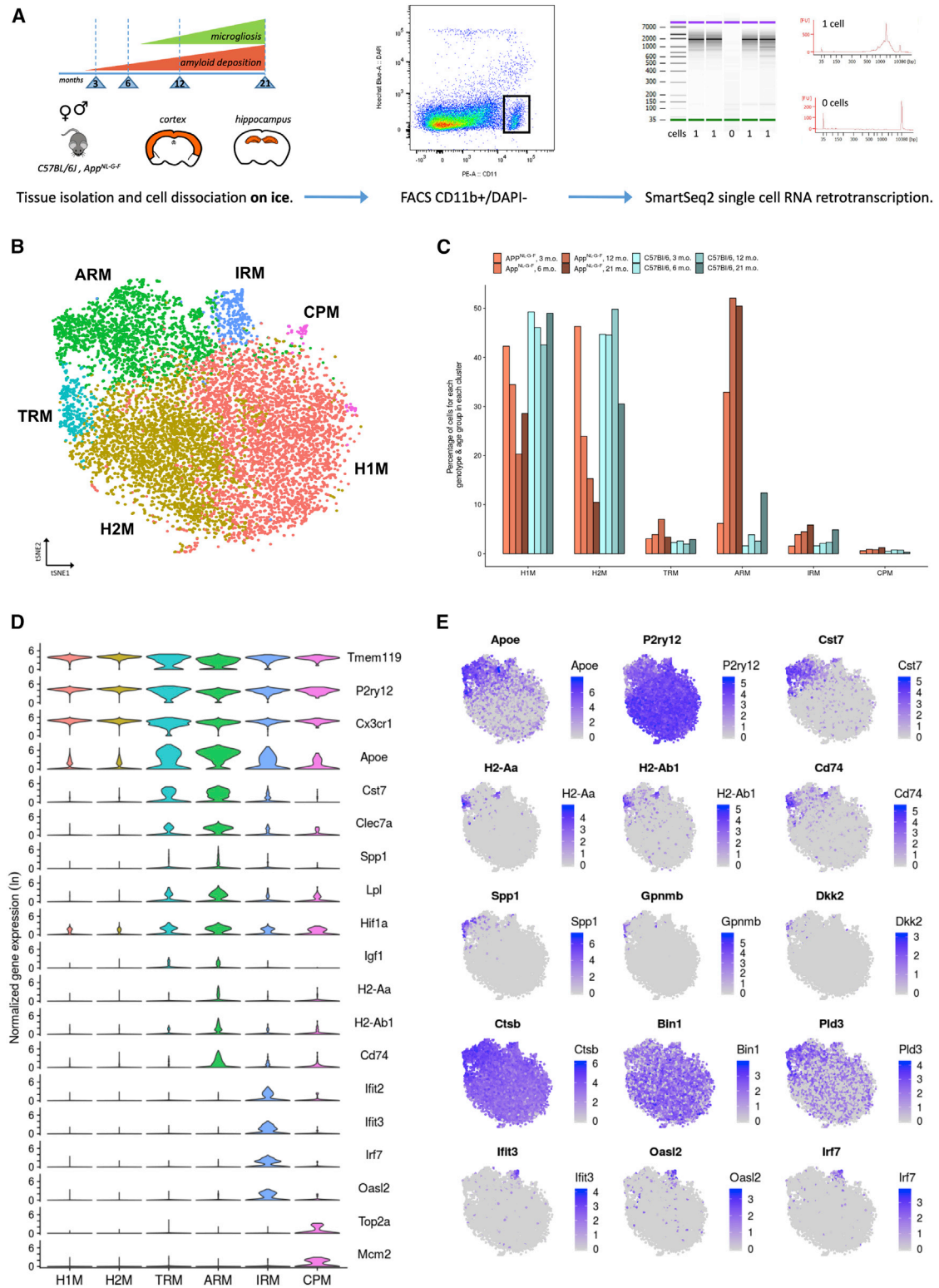
Figure 1. Microglia Mount a Heterogeneous Response to β-Amyloid, Marked by *Apoe* Overexpression

(A) Dataset presentation. We used male and female *App^NL-G-F* and wild-type *C57BL/6J* mice from four time points over the course of amyloid pathology and microgliosis as indicated. We dissected separately cortex and hippocampal tissues. The tissue from two animals for each experimental condition (age, sex,

(legend continued on next page)

patients, tilts the table from a rather benign Aβ proteopathy to the severe neurodegeneration with inflammation and Tau pathology that characterizes AD (De Strooper and Karran, 2016). In this regard, further understanding of the microglia response to amyloid pathology and the role of risk factors for AD in this response is key.

Several groups have applied high-throughput single-cell genomics and proteomics methods to characterize the shift in microglial cell states after different kinds of insults (Friedman et al., 2018; Hammond et al., 2019; Keren-Shaul et al., 2017; Mathys et al., 2017; Mrdjen et al., 2018). In neurodegenerative settings, microglia develop disease-associated phenotypes, such as the microglial neurodegenerative phenotype (MGnD) (Krasemann et al., 2017) or the disease-associated microglia (DAMs) (Keren-Shaul et al., 2017), but it is still an open question whether different subsets of such phenotypes exist, whether there are brain-area- or sex-specific differences in the microglial responses to Aβ, and which are the roles of AD risk genes expressed in microglia.

Here, we set out to address in a systematic way the question of how microglia respond over time, in cortex and hippocampus, to progressive Aβ deposition and whether this is affected by the three major risk factors for AD, i.e., age, sex, and genetics. We use an *App* knockin mouse model (App^{NL-G-F}), which displays progressive amyloidosis and microgliosis while avoiding overexpression of *APP* via artificial promotors (Masuda et al., 2016; Saito et al., 2014; Sasaguri et al., 2017) (Figure 1A). We show that the microglial responses to Aβ pathology are complex but, surprisingly, largely reproducible cell states that are also appearing during normal aging, albeit slower and quantitatively more limited. Moreover, we show that microglia in female mice tend to react earlier and in a more pronounced way than microglia in male mice, particularly in older mice. Interestingly, the major response of microglia to amyloid pathology is enriched for AD risk genes, with *Apoe* expression, in particular, becoming highly upregulated. This is partially confirmed in human tissue. Analysis of microglia from an $Apoe^{null}$ AD mouse model showed that the main Aβ response is severely impaired in the absence of *Apoe*.

RESULTS

We analyzed cortical and hippocampal microglia in female and male *C57BL/6J* wild-type and in App^{NL-G-F} mice at four different time points: at the beginning of Aβ deposition (3 months old

[m.o.]), at the beginning of overt histologically detectable microgliosis (6 m.o.), when both processes are well underway (12 m.o.), and at a late stage (21 m.o.) (Masuda et al., 2016) (Figure 1A). All together, we analyzed 32 different experimental conditions, taking into consideration the combinations of genotype, age, sex, and tissue (Figure 1A).

Tissue and cell suspensions were kept at <4°C during all steps of the isolation of microglia, to minimize artifactual activation (see STAR Methods). We isolated single live microglial cells (Cd11b+/DAPI−) by fluorescence-activated cell sorting (FACS) (Figure S1) and prepared single-cell full-length mRNA-sequencing libraries, using a modified SmartSeq2 method (Picelli et al., 2013, 2014; Trombetta et al., 2014) (see Figure 1A and STAR Methods). We sequenced a total of 12,024 single cells across the different experimental conditions. After quality control and removal of peripheral neutrophils (see Figure S2A and STAR Methods), we retained 10,801 microglial cells for further analysis.

Aging and Aβ Deposition Induce Similar Responses in Microglia

We next performed clustering analysis (see STAR Methods), which resulted in the identification of 6 major subpopulations of microglia (Figure 1B), displaying different abundances between genotypes and age groups (Figure 1C).

Two clusters expressing high levels of known homeostatic microglia markers (*Tmem119*, *P2ry12*, and *Cx3cr1*; Figure 1D) (Butovsky et al., 2014) dominated the whole microglial population (homeostatic 1 microglia and homeostatic 2 microglia; H1Ms and H2Ms, respectively; Figure 1B). In wild-type mice, H1Ms and H2Ms together accounted for 80%–90% of the total microglial population. They were roughly equally large at every time point, although H2Ms decreased by ∼10% in 21-m.o. mice (Figure 1C). In App^{NL-G-F} mice, both H1Ms and H2Ms were equally (>40% of all microglia each) represented at 3 months but then showed a drastic decrease with age over the course of pathology, particularly H2Ms (Figures 1C and S3A). Thus, H2Ms seem to be more sensitive to aging and amyloid pathology than H1Ms. H1Ms and H2Ms display subtle differences in expression of more than 700 genes, with statistically significant fold changes of 1.1–1.5 in either direction. While no clear gene expression signature differentiates the two subsets, genes such as *C1qa*, *C1qb*, *C1qc*, *Ctsb*, *Ctsd*, *Fth1*, and *Lyz2* were significantly upregulated in H2Ms. Therefore, the cluster of H2Ms, although displaying a canonical homeostatic gene

tissue, genotype) was pooled before microglia isolation. All procedures were performed on ice. Single live microglial cells were isolated by FACS (CD11b+, DAPI−), and single-cell RNA-sequencing (RNA-seq) libraries were prepared according to the SmartSeq2 and Nextera methods.

(B) t-distributed stochastic neighbor embedding (t-SNE) plot visualizing the 10,801 single microglial cells passing quality control after removal of peripheral cells. Cells are colored according to clusters identified with Seurat's k-nearest neighbors (kNN) approach (H1M and H2M, homeostatic microglia; TRM, transiting response microglia; ARM, activated response microglia; IRM, interferon response microglia; CPM, cycling and proliferating microglia).

(C) Percentage of cells from each genotype-age group for each cluster identified. App^{NL-G-F} cells are indicated in shades of red, while wild-type cells are indicated in shades of blue.

(D) Violin plots of selected marker genes for each identified cluster. The y axis indicates normalized gene expression (ln scale).

(E) t-SNE plots as in (B), colored by the level of ln normalized expression of selected genes. Clusters of TRMs and ARMs display increased expression of *Apoe* and inflammation markers (*Cst7*) and concurrently display a reduction of homeostatic markers (*P2ry12*). Two distinct regions of the ARMs cluster display increased expression of MHC class II genes (*H2-Aa*, *H2-Ab1*, and *Cd74*), suggesting the existence of microglial subpopulations. Further, a small subset of the ARMs cluster displays an enrichment for tissue repair genes (*Spp1*, *Gpnmb*, and *Dkk2*). The ARMs cluster also displays differential expression of several AD-related genes (e.g., *Ctsb*, *Bin1*, and *Pld3*) compared to clusters of H1Ms and H2Ms. The cluster of IRMs is enriched for interferon genes (*Ifit3*, *Oasl2*, and *Irf7*). See also Figure S5.
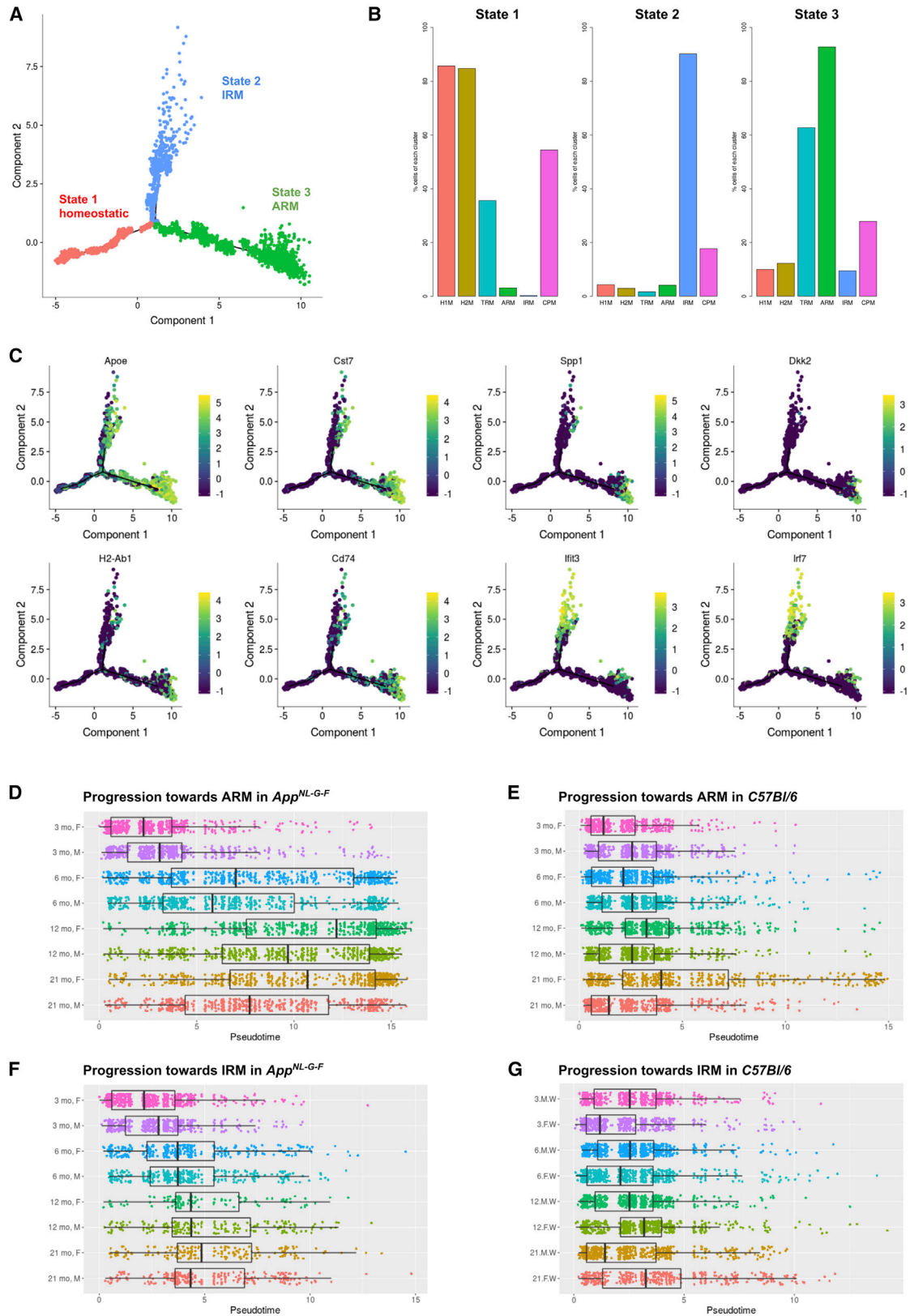
(legend on next page)

expression profile, seems more primed toward synapse pruning and heightened lysosomal activity and might therefore engage faster into more activated states. Interestingly, the clusters of H1Ms and H2Ms display a differential distribution relative to sex and tissue groups (Figures S3A–S3D). Therefore, our data uncover previously unrecognized heterogeneity in homeostatic microglia.

The other clusters were quite divergent from the homeostatic ones (Figure 1D). One cluster (ARMs; Figure 1B) increased strongly in the App^{NL-G-F} mice. It is characterized by the expression of gene sets involved in inflammatory processes (*Cst7*, *Clec7a*, and *Itgax*), in major histocompatibility complex (MHC) class II presentation (*Cd74*, *H2-Ab1*, *H2-Aa*, *Ctsb*, and *Ctsd*), and possibly involved in tissue regeneration (*Spp1*, *Gpnmb*, and *Dkk2*) (Figures 1D and 1E). A second cluster (TRMs; transiting response microglia; Figure 1B) has an overall transcriptomic profile similar to that of the ARMs cluster but had lower expression levels of *Apoe* and other inflammatory genes, particularly of MHC class II genes, while it did not express tissue regeneration genes (Figures 1D and 1E). A third cluster (IRMs [interferon response microglia]; Figure 1B) displayed a high expression of several genes involved in innate immune response and interferon response type I pathways (e.g., *Ifit2*, *Ifit3*, *Ifitm3*, *Irf7*, and *Oasl2*), which were otherwise not expressed in other clusters (Figures 1D and 1E). Finally, we identified a very small cluster of cells corresponding to 0.3%–1.2% of the total microglial pool (CPMs, cycling/proliferating microglia) (Figures 1B and 1C) that was enriched in genes involved in DNA replication, chromatin rearrangement, and cell cycle (e.g., *Top2a*, *Mcm2*, *Tubb5*, *Mki67*, and *Cdk*1) (Figure 1D). The cluster of CPMs did not display any selective enrichment for specific phenotypic groups (Figure 1C and S3A–S3D) and may represent a small pool of cycling microglia (Askew et al., 2017).

The proportion of cells in the clusters of reactive microglia (ARMs, TRMs, and IRMs) increased over age in both App^{NL-G-F} and wild-type mice (Figures 1C and S3A–S3D). Importantly, each cluster is present even in young wild-type mice (all together constituting 5.5% of the total wild-type microglia at 3 m.o.; Figure 1C), demonstrating that these clusters are physiological states of microglia. Although amyloid pathology does not induce a unique pathological microglial state in this animal model, there is, however, a very outspoken quantitative effect on the ARMs cluster, with 87% of the microglia in this cluster coming from App^{NL-G-F} mice. The number of ARMs increased 5-fold (6% to 33%) between 3 and 6 months, and by 12 months, they were

the major type of microglia (52%) in the App^{NL-G-F} mice, outnumbering the two homeostatic clusters. ARMs are, nevertheless, also increasing with aging in wild-type mice, reaching 12% of the total number of microglia at 21 months of age (Figure 1C). IRMs were present at a low percentage in both wild-type and App^{NL-G-F} mice, but their number increased over aging, particularly in App^{NL-G-F} mice (Figures 1C and S3A). Thus, aging alone induces transcriptome changes leading to two subtypes of activated microglia (ARMs and IRMs), and Aβ deposition enhances both cell states significantly.

Microglia Differentiate into Mutually Exclusive Response States

We wondered whether the different responses represented separate differentiation fates or consecutive steps on a continuous differentiation trajectory. Semi-supervised pseudotime analysis with Monocle 2 (Qiu et al., 2017a, 2017b; Trapnell et al., 2014) aligned microglial cells along a two-branched trajectory (Figure 2A). By identifying the distribution of cells from each cluster along these three branches, it becomes evident that homeostatic microglial cells (state 1) progressed either toward a state corresponding to the interferon-based IRMs response (state 2) or to a state corresponding to the heterogeneous ARMs response (state 3) (Figure 2A). This is quantitatively represented in Figure 2B, showing that 86% of homeostatic microglia (H1Ms and H2Ms) were retrieved in state 1, while 90% of the interferon response cells from the cluster of IRMs were in state 2, and 93% of the main Aβ-responsive ARMs cluster cells were in state 3 (Figure 2B; Figure S4). Cells from the cluster of TRMs were distributed between state 1 (36%) and state 3 (63%) (Figure 2B; Figure S4), further suggesting that this cluster represents cells transitioning between the two stages. The few cells in the cluster of CPMs were mostly found in state 1 (54%; 43 cells) but were represented also in state 2 (18%; 14 cells) and state 3 (28%; 22 cells) (Figure 2B; Figure S4).

Remarkably, *Apoe* expression continually increases along pseudotime in the ARMs (state 3) branch, together with several inflammatory markers (e.g., *Cst7*) (Figure 2C). MHC class II genes (e.g., *H2-Ab1* and *Cd74*) were predominantly expressed by cells toward mid-to-late pseudotime in the ARMs (state 3) branch (Figure 2C). Genes involved with tissue repair (e.g., *Spp1* and *Dkk2*) were expressed only by cells at the farthest end of the ARMs (state 3) branch (Figure 2C), which also expressed the highest *Apoe* levels, indicating that this subpopulation represents an advanced evolution of the microglial

Figure 2. Microglia Diversify into Two Cell State Branches during Response to β-Amyloid Plaques

(A) Plot of cell trajectories for all microglial cells, obtained by a semi-supervised pseudotime ordering with Monocle 2. Microglia are grouped into three stages (red: stage 1; blue: stage 2; green: stage 3). Homeostatic microglia (red) progress toward two separate fates: either the multifunctional ARMs response (green) or the IRMs response (blue).

(B) Percentage of cells from each cluster (Figure 1B) per state. The majority (>80%) of homeostatic microglia (clusters of H1Ms and H2Ms) are in state 1, the majority of interferon response cells (cluster of IRMs) are in state 2, and the majority of the activated response cells (cluster of ARMs) are in state 3.

(C) Expression levels of selected marker genes are plotted over a plot of cell trajectories, as in (A).

(D) Pseudotime progression plot of homeostatic App^{NL-G-F} microglial cells to the ARMs branches, presented separately for each age-gender experimental condition. Box represents the interquartile range, and the thick bar represents the group median.

(E) Pseudotime progression plot from homeostatic to ARMs for each wild-type microglial cell.

(F) Pseudotime progression plot from homeostatic to IRMs response for each App^{NL-G-F} microglial cell.

(G) Pseudotime progression plot from homeostatic to IRMs response for each wild-type microglial cell.

response. Most (94%) of these cells are derived from the App^{NL-G-F} mice. Although *Apoe* is also expressed in some interferon response (state 2) branch cells, its expression levels were lower compared to those in state 3 cells (Figure 2C), in agreement with differential expression analysis conducted at the cluster level (discussed earlier).

Differential expression analysis did not yield tissue- or sex-specific responses (Figures S3E and S3F), indicating that microglial responses to Aβ deposition is actuated stereotypically in hippocampus and cortex. Interestingly, female microglia displayed a faster progression in the deployment of the ARMs response in 6 m.o. App^{NL-G-F} and onward (Figures 2D–2G), which is reflected by the higher proportion of female ARMs cells compared to that of males (Figure S3B). Thus, although the response types and the genes involved are conserved between the two sexes, microglia in female mice appear to react earlier to Aβ.

ARMs Display Distinct Subpopulations Enriched for GWAS AD Risk Genes

Strikingly, *Apoe*, the main genetic risk factor for AD (Corder et al., 1993; Lambert et al., 2013), is strongly upregulated in ARMs, representing the major Aβ-response population (Figures 1D and 1E). Therefore, we wondered whether other AD risk genes are enriched among the genes that are differentially expressed (both up and down) in each of the reactive microglial clusters, compared to homeostatic microglia, using gene set enrichment analysis (GSEA) (Mootha et al., 2003; Subramanian et al., 2005). We used a list of genes associated with family history of AD from a recent extensive GWA study (GWAS) (Marioni et al., 2018). Taking into account that recent studies on polygenic risk scores show that genes with no genome-wide significance in GWASs still carry information with regard to risk of AD (Escott-Price et al., 2017), we decided to test for enrichment of GWAS genes at a number of different p value cutoffs (Figure 3A). For all tested p value cutoffs (ranging from p < $1e^{-6}$ to p < 0.01), only the ARMs cluster shows a strong enrichment for GWAS-associated AD genes (between p < $1e^{-6}$ and p < 0.005), suggesting that polygenic risk associates with the ARMs cell state. The GSEA algorithm yields a set of GWAS genes most responsible for the observed enrichment (which we refer to as the GWAS core enrichment genes). In our case, using the set with the strongest enrichment (p < $1e^{-5}$), these genes are the well-established AD risk genes *Apoe*, *H2-Eb1*, *Inpp5d*, *Bin1*, and *Ms4a6b* but also *Siglech* (or *CD33*) and *H2-Ab1*, which have been suggested to be associated with AD (Lambert et al., 2013). Interestingly, *Siglech*, *Inpp5d*, *Bin1*, and *Ms4a6b* were significantly downregulated in the ARMs cluster, while the others were significantly upregulated. Further work is needed to determine whether these changes act in a protective or harmful way, but it is known that a SNP in the *Siglech* locus suppressing *CD33* expression is protective in AD (Griciuc et al., 2013), while a SNP increasing its expression also increases AD risk (Bradshaw et al., 2013). We further looked specifically at the expression level (Figure S5) of a list of AD-related genes (Table S2) compiled from an extensive literature review. The expression levels of cathepsins *Ctsb* and *Ctsd*, *Trem2* and *Tyrobp*, *H2-Eb1*, *Pld3*, and *Aplp2* were all

significantly upregulated in the ARMs cluster, while *Adam10*, *Bin1*, *Cass4*, *Cd33*, *Ctsf*, *Inpp5d*, *Ms4a6d*, and *Picalm* showed decreased expression in the same cluster (Figure S5).

We next investigated the genes upregulated in the ARMs cluster relative to the homeostatic cluster in bulk tissue from human brains obtained from the Accelerating Medicines Partnership-AD (AMP-AD) portal (Hodes and Buckholtz, 2016). 62 of the top 100 genes upregulated in the ARMs cluster were also significantly (adjusted p < 0.05) upregulated in subjects with high plaque burden (Consortium to Establish a Registry for AD [CERAD] stage C3) compared to the stage-C0 subjects. The parahippocampal region from the Mount Sinai Brain Bank (MSBB) cohort region had the highest number of differentially expressed genes, with *TREM2*, *ITGAX*, and *CD74* displaying the highest effect sizes (Figure 3D). Some of the GSEA core enrichment genes were also significantly upregulated in C3 subjects: *HLA-DRB5*, *HLA-DQA1*, and *HLA-DQB1* (orthologs of *H2-Eb1* and *H2-Ab1*) (Figure 3D). We then sought to determine whether these expression changes due to plaque increase were independent of the presence of tangles. To test this hypothesis, we analyzed gene expression between subjects with different plaque load and without tangles (Braak stages 0, I, and II), the human conditions most analogous to App^{NL-G-F} mice. The top genes that increased with plaque mean score were *TREM2*, *TYROBP*, and *CD68* in the MSBB parahippocampal dataset, with *TREM2* displaying a 2.7-fold increase (p = 0.2 · 10^{-4}).

As indicated earlier, the ARMs from App^{NL-G-F} mice do not appear as one homogeneous cluster. Therefore, we assessed whether we could further subdivide the ARMs cells. In Figure 3B, we visualized the signature score (see STAR Methods) for the up-regulated GWAS core enrichment genes, showing two sub-clusters within the ARMs cluster (labeled "A" and "B" in Figure 3B). Both subclusters are highly enriched (96%) for App^{NL-G-F} cells, suggesting that these particular subsets of ARMs might constitute specific responses to Aβ accumulation. The ARMs A subcluster expresses typical ARMs genes, along with genes possibly involved in tissue repair and remyelination, e.g., *Spp1* (osteopontin, a chemoattractant and an adhesion protein involved in wound healing), *Gpnmb* (osteoactivin, involved in extracellular matrix remodelling), and *Dkk2* (a secreted Wnt pathway antagonist) (Figure 1E). The ARMs B subcluster expresses *Tmem119* but no genes overexpressed by other ARMs (e.g., *Spp1*, *Lpl*, *Gpnmb*, *Apoe*, *Clec7a*, and *Cst7*) (Figure 1E). Thus, in App^{NL-G-F} mice, Aβ boosts the heterogeneous ARMs response, with a gene signature that is enriched with AD risk genes, and elements of which can be retrieved in human subjects displaying a high plaque load.

Apoe-Expressing Microglia Cluster around β-Amyloid Plaques

We were particularly intrigued by the high expression of *Apoe* in ARMs. As *Apoe* is mainly expressed by astrocytes in non-pathological conditions, we wondered whether astrocytes would also increase *Apoe* expression upon exposure to Aβ plaques. We performed single-molecule fluorescence *in situ* hybridization (smFISH) with RNAscope probes against *Apoe* and *Itgam* or *Slc1a3* to mark microglia and astrocytes, respectively.
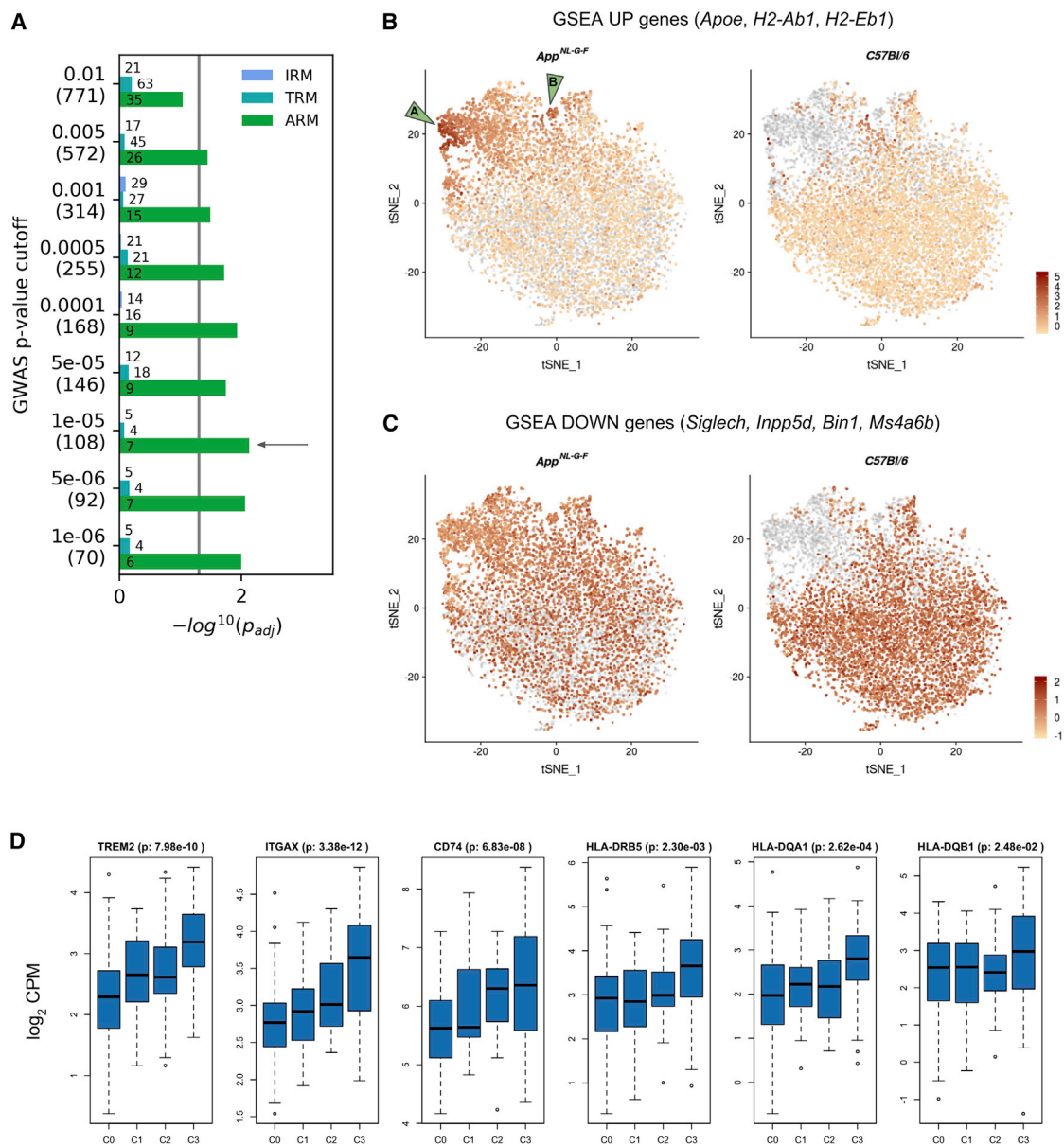
Figure 3. Enrichment Analysis of AD Genes Highlights Substructures of ARMs

(A) Bar plot showing the significance ($-\log_{10}$ p value adjusted for false discovery rate; p_{adj}) of enrichment of AD GWAS genes among the genes differentially expressed in each of the three reactive microglial clusters (IRMs, TRMs, and ARMs) compared to the homeostatic microglia (H1Ms + H2Ms), calculated using GSEA. A significant enrichment indicates that more AD GWAS genes than expected are found among genes most strongly affected in the differential expression analysis for each comparison. We tested a number of different AD GWAS sets using different p value cutoffs: the numbers in the parentheses indicate the number of genes for that specific cutoff. The numbers in the bars indicate the size of the GSEA-predicted leading edge (core enrichment genes), which can be interpreted as the genes responsible for the observed enrichment. The enrichment for the p < $1e^{-5}$ cutoff yielded the lowest p_{adj}.

(B and C) Of the 7 core enrichment genes for the p < $1e^{-5}$ cutoff, 3 (*Apoe*, *H2-Ab1*, and *H2-Eb1*) were upregulated in ARMs compared to homeostatic microglia, while 4 genes (*Siglech*, *Inpp5d*, *Bin1*, and *Ms4a6b*) were downregulated. For each set of up- and downregulated core enrichment genes, we calculated a signature score (i.e., a composite expression score of a set of genes) using Seurat's *AddModuleScore* function. Each cell's score for either the upregulated (B) or downregulated (C) gene set is visualized on a t-SNE plot (as in Figure 1B). In both cases, cells of the two genotypes are plotted separately, as indicated in the titles, with cells of the other genotype plotted in gray. In (B), the App^{NL-G-F} cells clearly display a strong signature score for AD GWAS genes showing in the ARMs cluster. The two green arrowheads on the left in (B) indicate two areas with particularly strong expression of these genes.

(D) Boxplots of gene expression across CERAD stages in the parahippocampal brain region from the MSBB cohort. The adjusted p values of CERAD score C3 (Alzheimer's disease) versus C0 comparisons are displayed next to the gene names. Similar results were found in the ROSMAP dataset (data not shown).
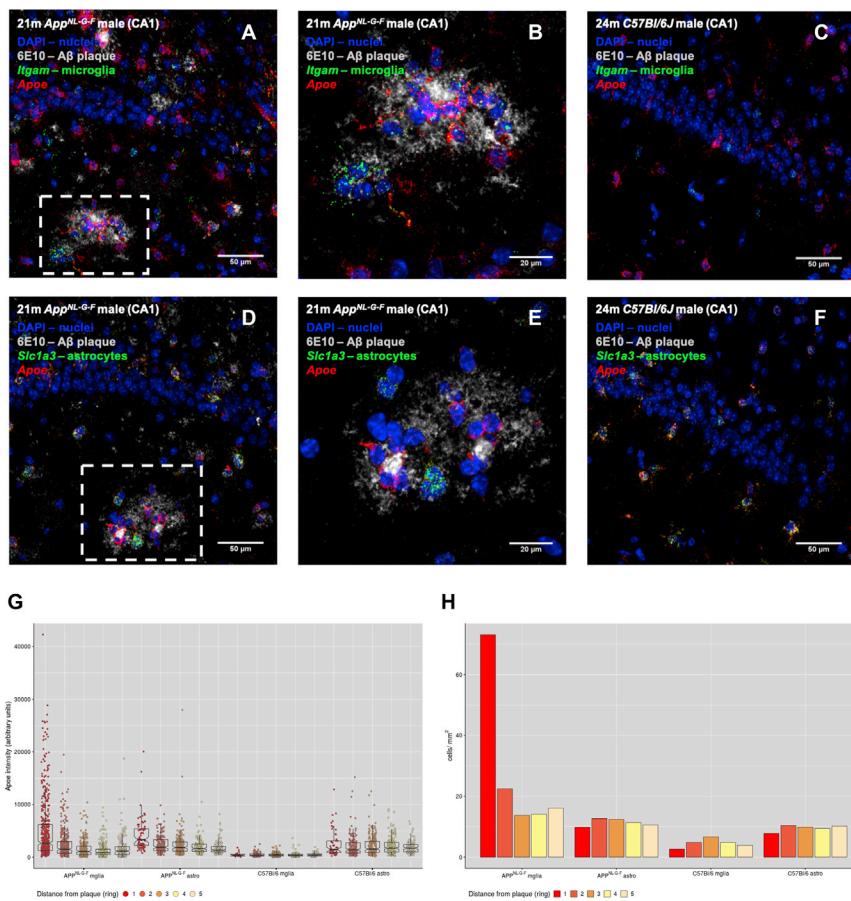
Figure 4. Microglia Are the Major Contributors of *Apoe* Expression in the Vicinity of β-Amyloid Plaques

(A–F) Combined RNAscope and immunofluorescent analyses of *Apoe* expression by microglia and astrocytes in the vicinity of β-amyloid plaques. Expressions of *Apoe*, the microglia marker *Itgam* (A–C), and the astrocyte marker *Slc1a3* (D and E) were visualized using RNAscope probes, while plaques were visualized by staining with the anti-Aβ antibody 6E10. Nuclei were visualized with DAPI. Photos are representative of three mice per genotype. (A and D) are representative images of *App*$^{NL-G-F}$ CA1 stained for microglia (*Itgam*) and astrocytes (*Slc1a3*), respectively. (B) Zoom-in of the boxed area in (A), taken as a separate image with a higher magnification lens. Similarly, (E) is a zoom-in of the boxed area in (D). (C) and (D) are representative images of male wild type *C57Bl/6J* CA1, stained for microglia (*Itgam*) and astrocytes (*Slc1a3*), respectively. Scale bars in (A), (C), (D), and (F) represent 50 μm, while in (B) and (E) represent 20 μm.

(G) Quantification of *Apoe* staining intensity per cell, classified based on the genotype (*App*$^{NL-G-F}$ or *C57BL/6J*), cell type (microglia [mglia] or astrocyte [astro]), and distance from a plaque (ring). For wild-type mice, measurements were made by selecting random regions of interest (ROIs) in the same brain areas as in *App*$^{NL-G-F}$. Measurements were made from at least 25 plaques or ROIs for each condition (*App*$^{NL-G-F}$ mglia, *C57BL/6J* mglia, *App*$^{NL-G-F}$ astro, and *C57BL/6J* astro), collected from 3 mice per genotype.

(H) Number of microglia and astrocytes next to plaques. As in (G), cells were classified based on genotype and distance from plaques (*App*$^{NL-G-F}$) or random ROIs (*C57BL/6J*).

smFISH was coupled with immunofluorescent detection of Aβ plaques using 6E10 antibody (Figures 4A–4F). *Itgam* and *Apoe* signals strongly colocalized in cells associated with plaques, while this was rare in cells located further away from plaques (Figures 4A, 4B, and 4G). Staining with the astrocyte marker *Slc1a3* (Figures 4D and 4E) confirmed that astrocytes, but no microglia, were expressing *Apoe* in wild-type mice (Figures 4C and 4F).

We quantified the intensity of *Apoe* staining in microglia and astrocytes at different distances from plaques. The intensity of *Apoe* staining gradually increased in both cell types when closer to plaques, but the increase was much higher in microglia than in astrocytes (Figure 3G). Microglia, furthermore, were clustered around Aβ plaques, while astrocytes were evenly distributed across the tissue (Figure 4H).

These results indicate that microglia constitute the main cellular response close to plaques and that ApoE production at plaques is mainly of microglial origin. We did not see an increase of cycling cells (cluster of CPMs) in *App*$^{NL-G-F}$ mice, suggesting that the increased number of microglia next to plaques is not due to increased proliferation and represents likely the evolution of microglia from homeostatic H1 and H2 to reactive ARMs cell states in *App*$^{NL-G-F}$.

Deletion of *Apoe* Suppresses the Microglial Response to β-Amyloid

We wondered whether *Apoe* was directly involved in the microglial responses to Aβ pathology. An *Apoe*^{null} mouse strain is not available on an *App*$^{NL-G-F}$ background at this moment; therefore, we used a second AD mouse model (*APP/PS1*) for which an *Apoe*^{null} strain has been recently developed (*APP/PS1-Apoe*^{null}; [E.H., J. Klickstein, C. Cannavo, R. Jackson, A. Muzikansky, S. Gandhi, D. Urick, T. Sargent, L. Wrobleski, A.D. Roe, S., Hou, K.V. Kuchibhotla, R.A. Betensky, T. Spires-Jones, B.T. Hyman, unpublished data]). We sequenced 2,304 single cells from 18-m.o. male *APP/PS1* and *APP/PS1-Apoe*^{null} mice and from the respective control strains, *C57BL/6J* and *C57BL/6J-Apoe*^{null}. After quality control and removal of peripheral neutrophils (Figure S6), we retained 1,880 microglial cells for further analysis. Clustering analysis of cells from all four genotypes identified 4 major microglial populations (Figure 5A, middle) and was consistent with a similar analysis performed after removal of *Apoe* from the original gene count matrix (data not shown).

We confirmed that the overall microglial responses in *APP/PS1* mice were similar to those seen in *App*$^{NL-G-F}$ mice. The major cluster displayed high expression of homeostatic genes
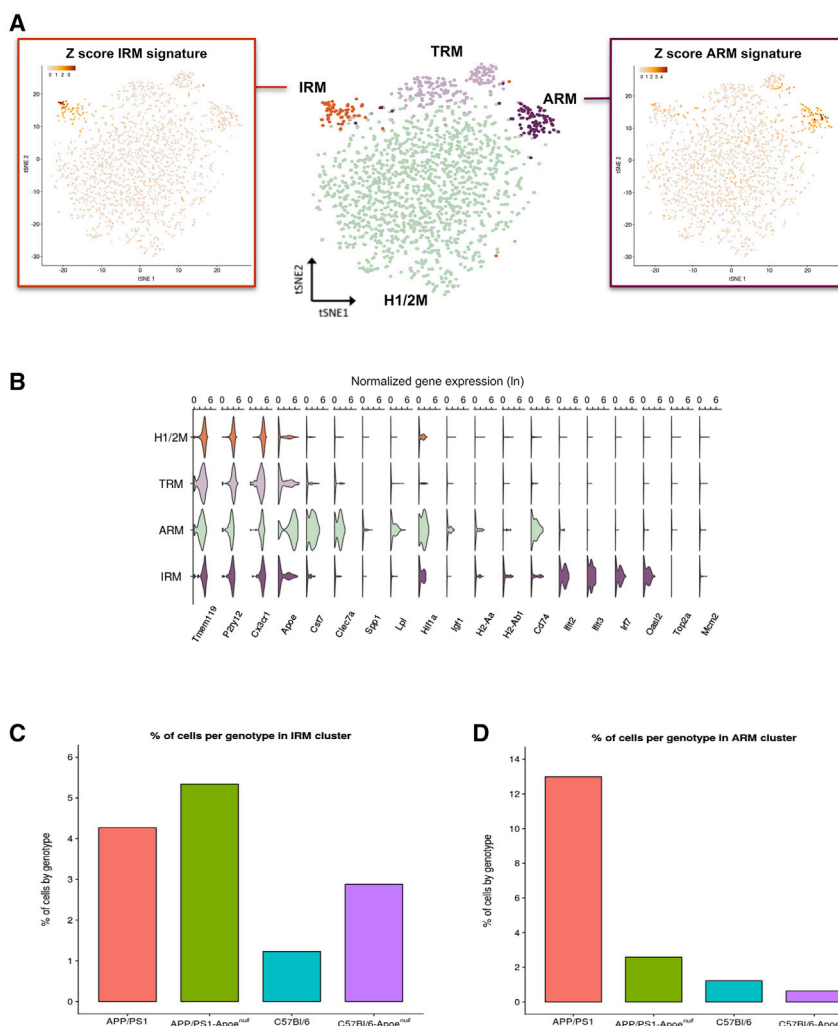
Figure 5. *Apoe* Deletion Prevents the Establishment of a Main Inflammatory Response to β-Amyloid Plaques

Analysis by single-cell RNA-seq of single live microglial (CD11b+/DAPI−) cells, prepared as described in Figure 1A, from *APP/PS1* and *APP/PS1-Apoe^null* mice and their respective wild-type control strains *C57BL/6J* and *C57BL/6J-Apoe^null*.

(A) Middle: t-SNE plot visualizing the 1,880 single microglial cells passing quality control after removal of peripheral cells. Cells are indicated according to clusters identified with Seurat's kNN approach (H1/2M, homeostatic microglia; TRM, transiting response microglia; ARM, activated response microglia; IRM, interferon response microglia). Left: t-SNE plot as in the middle, colored by the Z-score of gene signatures for the interferon response (IRM). Right: t-SNE plot as in the middle, colored by the *Z* score of gene signatures for the activated response (ARM).

(B) Violin plots of selected marker genes for each identified cluster. The x axis indicates normalized gene expression (ln scale).

(C) Percentages of cells from each mouse genotype in the IRMs cluster.

(D) Percentages of cells from each mouse genotype in the ARMs cluster.

IRMs cells showed only a moderate increase in *Apoe* expression (Figure 2C).

Plaques of *APP/PS1* mice appear bigger and more amorphous compared to plaques in *App^NL-G-F* mice (Figures 6A and 6B), as evidenced elsewhere (E.H., J. Klickstein, C. Cannavo, R. Jackson, A. Muzikansky, S. Gandhi, D. Urick, T. Sargent, L. Wrobleski, A.D. Roe, S., Hou, K.V. Kuchibhotla, R.A. Betensky, T. Spires-Jones, B.T. Hyman, unpublished data). In both *App^NL-G-F* and *APP/PS1* mice, plaques are stained heavily for ApoE, and microglia appear to develop ramifications and to invade plaques (Figures 6A and 6B). Lack of *Apoe* expression did not alter the global amyloid burden (Figures 6B, 6D, and 6E); however, it caused a significant decrease in the amounts of Metoxy-XO4-stained amyloid (Figure 6F), as previously reported for other *Apoe^null* AD mouse models (Holtzman et al., 2000; Irizarry et al., 2000; Krasemann et al., 2017; Ulrich et al., 2018), with a consequent shift of the total versus dense core amyloid ratio (Figure 6G). Moreover, lack of ApoE causes a significant decreased density of microglial cells around amyloid deposits (p < 0.001; Figure 6H). Thus, ApoE, next to be involved in amyloid aggregation, also appears required to mount a full ARMs transcriptional response against Aβ plaques.

DISCUSSION

Our data show previously unrecognized heterogeneity in both homeostatic and reactive microglia. We identified two populations of homeostatic microglia (H1Ms and H2Ms), which display
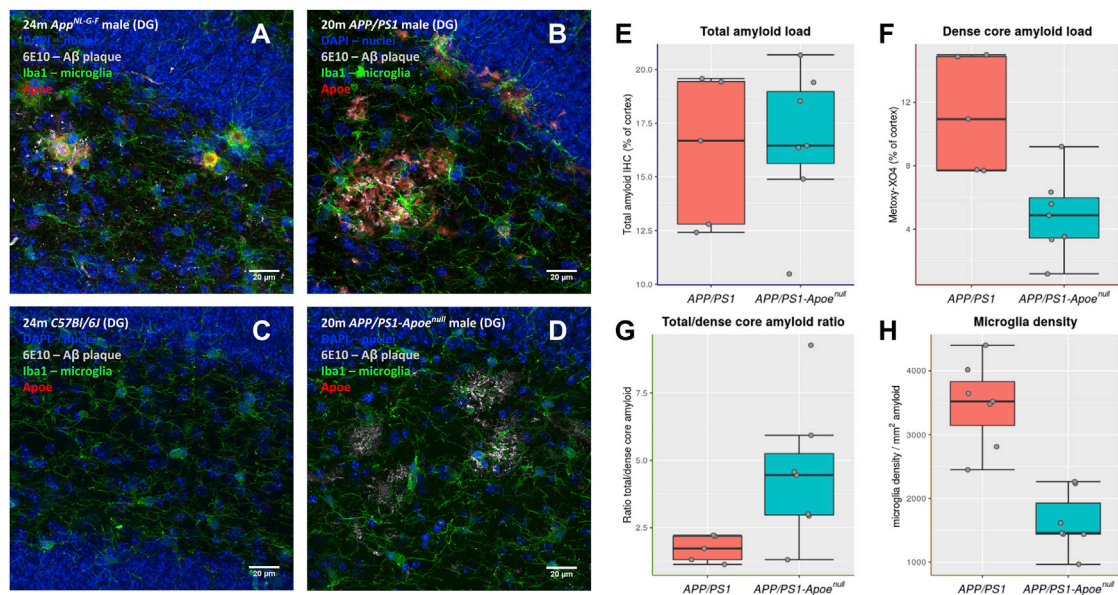
(Figure 5B) (H1/2M [homeostatic microglia 1 and 2]; Figure 5A). A second cluster displayed a high score for the ARMs signature (ARMs cluster; Figure 5A, right), while a third cluster displayed high scores for the interferon response signature (IRMs cluster; Figure 5A, left). A fourth cluster displayed high levels of homeostatic genes but also a higher ARMs score compared to that of cluster H1/2M, thus representing a transiting state between H1/2M and ARMs (TRMs cluster; Figure 5A). Notably, the ARMs cluster was strongly enriched for *APP/PS1* microglia (15% of all *APP/PS1* microglia; p = 0.08e−10) but contained only very few (2%) *APP/PS1-Apoe^null* cells (Figure 5D). Conversely, *APP/PS1-Apoe^null* mice showed 6% cells in the IRMs cluster versus 3% of microglia in *APP/PS1* mice (Figure 5C). Thus, deletion of *Apoe* impairs the normal deployment of the ARMs response but does not block the IRMs response. Moreover, lack of *Apoe* boosted the interferon-type response independently of Aβ deposition, as *C57BL/6J-Apoe^null* showed a tendency for a higher percentage of IRMs compared to *C57BL/6J* mice (2.9% versus 1.2%, respectively) (Figure 5C). This is in agreement with gene expression data from *App^NL-G-F* mice, which displayed high levels of *Apoe* in ARMs cells, while

Figure 6. Lack of *Apoe* Prevents Migration of Microglia toward Plaques

(A–D) Immunofluorescent staining of microglia (Iba1, green), ApoE (red), and Aβ plaques (6E10, white) in sagittal sections of App^{NL-G-F} (A), *APP/PS1* (B), *C57BL/6J* (C), and *APP/PS1-Apoe^{null}* (D). Images are zoomed on the dentate gyrus (DG) region. Scale bars represent 20 μm.

(E–G) Analysis of amyloid burden in 18- to 20-m.o. *APP/PS1* and *APP/PS1-Apoe^{null}* mice. Total amyloid burden as detected by anti-Aβ immunostaining (E), dense core plaque burden identified by Metoxy-XO4 staining (F), and the ratio between total amyloid burden and dense core plaques (G) are presented as boxplots (boxes represent the 25%–75% quartile range; whiskers represent the ±1.5 interquantile range; each experimental point is represented by a gray dot; n = 5–7 mice per group; *p < 0.05, Mann-Whitney test).

(H) Stereological evaluation of the density of Iba-1 reactive microglia around amyloid deposits in *APP/PS1* and *APP/PS1-Apoe^{null}* mice; boxplot is as in (E), n = 5–7 mice per group. **p < 0.001, Mann-Whitney test.

subtle but significant gene expression differences and are differentially enriched in different brain areas and in female compared to male mice. The separation in these two clusters is relevant, as H2Ms cells also decline more rapidly than H1Ms cells with aging. We identified also two major populations of reactive microglia. One displays a multifunctional gene response that we call here the ARMs response. Although the ARMs response overlaps with the DAMs response described by Keren-Shaul et al. (2017), we provide evidence that these cells are part of the normal evolution of microglia in healthy aging, and we find the term "disease associated" misleading. In fact, ARMs cells are already detected in the brains of wild-type mice at young ages, further underlining that they are not necessarily disease associated. The presence of amyloid plaques in App^{NL-G-F} mice boosts the redistribution of homeostatic microglia to ARMs cells, which eventually become the predominant population. At odds with the original DAMs response description is also the heterogeneity in the ARMs group uncovered here: several subpopulations can be discerned by the expression of specific subsets of genes, such as genes involved in MHC class II presentation (*H2-Ab1*, *H2-Aa*, and *Cd74*) and genes potentially involved in tissue repair (*Spp1*, *Gpnmb*, and *Dkk2*). These subsets are highly enriched for App^{NL-G-F} microglia, suggesting that they could represent an exaggerated or modified response to the plaques and that these sub-responses might provide the real pathological signature of microglia in AD.

The second population of reactive microglia is enriched for interferon response genes and therefore called the IRMs response. IRMs are again present in wild-type and App^{NL-G-F} mice in all age groups and, therefore, again part of the normal physiological heterogeneity of microglia in the healthy mouse brain. The IRMs population is much less affected by the presence of amyloid plaques than the ARMs population. Interestingly, gene enrichment analysis indicates that ARMs, but not IRMs, are enriched for known AD risk genes such as *Apoe*, *Trem2*, *Tyrobp* (DAP12), *Ctsb*, *Ctsd*, *H2-Eb1*, and *Pld3* (Cruchaga and Goate, 2015a, 2015b; Cruchaga et al., 2014; Fazzari et al., 2017; Heilmann et al., 2015; Hooli et al., 2015; Lambert et al., 2015; van der Lee et al., 2015). This strongly argues that the role of these genetic risk factors in AD is in the activation and function of this specific microglia subpopulation.

Microglia expressing interferon response genes have been described as a late response to neurodegeneration in a CK-p25 model (Mathys et al., 2017); however, these look quite different from the IRMs described here. For example, IRMs do not co-express MHC genes and, as stated earlier, are present also in healthy, normal brain, even at a young age. It should be noted that CK-p25 induces a rapid and severe neurodegeneration that might be different mechanistically from the very slow and mild disease caused in App^{NL-G-F} mice by Aβ deposition. App^{NL-G-F} mice are regarded as models of early AD pathology.

Pseudotime analysis is a good way to investigate how different microglial expression profiles relate to each other (Trapnell et al., 2014). This analysis suggests that the different cell states we describe here are, in fact, part of a continuous spectrum, with homeostatic microglia (H1Ms and H2Ms) adapting two major response branches, IRMs and ARMs, which increase during aging and especially upon exposure to Aβ. These branching trajectories broadly match the old classification of microglia as resting (M0), pro-inflammatory (M1), and pro-resolution (M2) microglia, but they also indicate that microglial phenotypes are highly dynamic (Butovsky and Weiner, 2018; Friedman et al., 2018; Keren-Shaul et al., 2017; Mrdjen et al., 2018; Ransohoff, 2016).

Heterogeneity of microglia between different brain areas (Grabert et al., 2016) and between different sexes (Villa et al., 2018) is increasingly recognized. We show here, however, that the response to Aβ deposition evolves stereotypically across brain areas (cortex and hippocampus) in animals of both sexes. Remarkably, we show that microglia in female mice progress faster over the ARMs trajectory compared to microglia in male mice (Figure 2D). This is in agreement with previous histological analysis (Masuda et al., 2016). Such sex-dependent differences in microglial responses are interesting to note, as there is a higher incidence of AD in women (Ferretti et al., 2018; van der Flier and Scheltens, 2005; Laws et al., 2018; Mazure and Swendsen, 2016).

We demonstrate here, in agreement with previous findings (Keren-Shaul et al., 2017; Krasemann et al., 2017), that ARMs induce *Apoe* expression up to 27-fold, compared to homeostatic microglia. In particular, in proximity to plaques, microglia express higher levels of *Apoe* than astrocytes (∼2.3-fold higher median *Apoe* intensity per cell; Figure 3G). We show also that *Apoe* is not merely a marker for this cell state but is a key component of the ARMs response, as its deletion severely reduces the number of microglia displaying an ARMs signature (Figure 4) and affects the interaction of microglia with Aβ plaques (Figure 5). Given this spectacular influence of *Apoe* expression on the phenotype of microglia, we speculate that a large part of the genetic risk associated with the *APOE4* genotype (Corder et al., 1993; Rebeck et al., 1993) is likely executed via modification of the microglial function rather than other mechanisms. While we cannot exclude that the abnormal plaques that are generated in the absence of ApoE affect the microglia response, it seems more likely that ApoE directly modulates the response of the microglia to the plaques and that ApoE is responsible for the induction of the ARMs response to amyloid, likely by interacting with Trem2 (Yeh et al., 2016). Thus, the major genetic risk factor for AD, together with most other identified risk genes in GWASs, modulates the neuroinflammatory response of the microglia to amyloid plaques.

Our observation that many AD GWAS-associated genes appear to change their expression in the ARMs indicates an overlap between the pathogenesis of AD in humans and the microglial response to the accumulation of amyloid in the brain of the mouse models. Thus, these GWAS variants, when present in a patient, likely affect the way that microglia cope with the accumulation of amyloid over age. In that capacity, they might either exacerbate or act protectively with regard to the onset of the disease. Such a view predicts that patients with a high load of amyloid but with a protective combined polygenic risk score (which, in the case of AD, covers mostly genes expressed in microglia) will respond in a beneficial way to amyloid and will not develop full-blown AD.

In conclusion, our data refine the concepts of homeostatic and reactive microglia and indicate that major AD risk factors (age, sex, and APOE) link to a multifunctional and complex microglial response to amyloid plaques that evolves over different branches of a continuous spectrum of molecular phenotypes. The complex response of the microglia, even when described as a unique cell state, "ARMs," is probably not so surprising, as the responses of individual microglia will likely profoundly depend on factors in the microenvironment of the plaques requiring differential functions of the microglial toolkit to be engaged. A particular challenge for the future is to dissect the distribution of different ARMs subpopulations over the brain and to add functional significance to the different gene expression patterns. It is likely that such functional dissection will lead to a whole set of novel drug targets that each will be useful in modulating a microglial response that is most beneficial for AD.

STAR★METHODS

Detailed methods are provided in the online version of this paper and include the following:

- KEY RESOURCES TABLE
- CONTACT FOR REAGENT AND RESOURCE SHARING
- EXPERIMENTAL MODELS DETAILS
  - Mice
- METHOD DETAILS
  - Single cell suspension preparation
  - Single microglia isolation by FACS
  - Single cell mRNA libraries preparation and sequencing
  - Sequencing data analysis
  - Human RNAseq data analysis
  - Multiplex RNAscope and immunofluorescence staining
  - RNAscope image analysis and quantification
  - Immunofluorescence staining
  - Amyloid load analysis
- QUANTIFICATION AND STATISTICAL ANALYSIS
  - Differential gene expression
  - RNAscope signal quantification and cell count
  - Stereological quantification of amyloid burden and microglia density
- DATA AND SOFTWARE AVAILABILITY

AUTHOR CONTRIBUTIONS

C.S.F. and B.D.S. conceptualized and designed the study and the experiments. C.S.F. optimized methods with L.W. and analyzed and interpreted single-cell sequencing and imaging data. L.W. isolated microglia, prepared single-cell RNA-sequencing libraries, performed *in situ* RNA hybridization and immunofluorescent staining, and analyzed and interpreted *in situ* data. I.V. and I.S. performed *in situ* RNA hybridization and immunofluorescent staining and analyzed and interpreted imaging data. N.F., N.T., W.-T.C., M.E.W., G.S., and M.F. analyzed and interpreted single-cell RNA-sequencing data. E.H. performed amyloid burden analysis. S.D. analyzed human RNA-sequencing data. R.M., T.M., E.K., B.H., and V.H.P. interpreted data. T.S. and B.H. contributed animals. B.D.S. procured funding and interpreted data. The manuscript was written by C.S.F. and B.D.S., with input from all co-authors. All co-authors read and approved the final version of the manuscript.

DECLARATION OF INTERESTS

REFERENCES

Allen, M., Carrasquillo, M.M., Funk, C., Heavner, B.D., Zou, F., Younkin, C.S., Burgess, J.D., Chai, H.-S., Crook, J., Eddy, J.A., et al. (2016). Human whole genome genotype and transcriptome data for Alzheimer's and other neurodegenerative diseases. Sci. Data *3*, 160089.

Askew, K., Li, K., Olmos-Alonso, A., Garcia-Moreno, F., Liang, Y., Richardson, P., Tipton, T., Chapman, M.A., Riecken, K., Beccari, S., et al. (2017). Coupled proliferation and apoptosis maintain the rapid turnover of microglia in the adult brain. Cell Rep. *18*, 391–405.

Bateman, R.J., Xiong, C., Benzinger, T.L.S., Fagan, A.M., Goate, A., Fox, N.C., Marcus, D.S., Cairns, N.J., Xie, X., Blazey, T.M., et al.; Dominantly Inherited Alzheimer Network (2012). Clinical and biomarker changes in dominantly inherited Alzheimer's disease. N. Engl. J. Med. *367*, 795–804.

Behl, C., and Ziegler, C. (2017). Beyond amyloid—widening the view on Alzheimer's disease. J. Neurochem. *143*, 394–395.

Bihlmeyer, N.A., Merrill, E.M., Lambert, Y., Srivastava, G.P., Clark, T.W., Hyman, B.T., and Das, S. (2019). Novel Methods for Integration and Visualization of Genomics and Genetics Data in Alzheimer's Disease. Alzheimers Dement. Published online March 29, 2019. https://doi.org/10.1016/j.jalz.2019.01.011.

Borchelt, D.R., Ratovitski, T., van Lare, J., Lee, M.K., Gonzales, V., Jenkins, N.A., Copeland, N.G., Price, D.L., and Sisodia, S.S. (1997). Accelerated amyloid deposition in the brains of transgenic mice coexpressing mutant presenilin 1 and amyloid precursor proteins. Neuron *19*, 939–945.

Bradshaw, E.M., Chibnik, L.B., Keenan, B.T., Ottoboni, L., Raj, T., Tang, A., Rosenkrantz, L.L., Imboywa, S., Lee, M., Von Korff, A., et al.; Alzheimer Disease Neuroimaging Initiative (2013). CD33 Alzheimer's disease locus: altered monocyte function and amyloid biology. Nat. Neurosci. *16*, 848–850.

Butler, A., Hoffman, P., Smibert, P., Papalexi, E., and Satija, R. (2018). Integrating single-cell transcriptomic data across different conditions, technologies, and species. Nat. Biotechnol *36*, 411–420.

Butovsky, O., and Weiner, H.L. (2018). Microglial signatures and their role in health and disease. Nat. Rev. Neurosci. *19*, 622–635.

Butovsky, O., Jedrychowski, M.P., Moore, C.S., Cialic, R., Lanser, A.J., Gabriely, G., Koeglsperger, T., Dake, B., Wu, P.M., Doykan, C.E., et al. (2014). Identification of a unique TGF-β-dependent molecular and functional signature in microglia. Nat. Neurosci. *17*, 131–143.

Calderon, D., Bhaskar, A., Knowles, D.A., Golan, D., Raj, T., Fu, A.Q., and Pritchard, J.K. (2017). Inferring relevant cell types for complex traits by using single-cell gene expression. Am. J. Hum. Genet. *101*, 686–699.

Corder, E.H., Saunders, A.M., Strittmatter, W.J., Schmechel, D.E., Gaskell, P.C., Small, G.W., Roses, A.D., Haines, J.L., and Pericak-Vance, M.A. (1993). Gene dose of apolipoprotein E type 4 allele and the risk of Alzheimer's disease in late onset families. Science *261*, 921–923.

Cruchaga, C., and Goate, A.M. (2015a). Cruchaga & Goate reply. Nature *520*, E5–E6.

Cruchaga, C., and Goate, A.M. (2015b). Cruchaga & Goate reply. Nature *520*, E10.

Cruchaga, C., Karch, C.M., Jin, S.C., Benitez, B.A., Cai, Y., Guerreiro, R., Harari, O., Norton, J., Budde, J., Bertelsen, S., et al.; Alzheimer's Research UK (ARUK) Consortium (2014). Rare coding variants in the phospholipase D3 gene confer risk for Alzheimer's disease. Nature *505*, 550–554.

De Strooper, B., and Karran, E. (2016). The cellular phase of Alzheimer's disease. Cell *164*, 603–615.

Dobin, A., Davis, C.A., Schlesinger, F., Drenkow, J., Zaleski, C., Jha, S., Batut, P., Chaisson, M., and Gingeras, T.R. (2013). STAR: ultrafast universal RNA-seq aligner. Bioinformatics *29*, 15–21.

Escott-Price, V., Shoai, M., Pither, R., Williams, J., and Hardy, J. (2017). Polygenic score prediction captures nearly all common genetic risk for Alzheimer's disease. Neurobiol. Aging *49*, 214, e7–214.e11.

Fazzari, P., Horre, K., Arranz, A.M., Frigerio, C.S., Saito, T., Saido, T.C., and De Strooper, B. (2017). PLD3 gene and processing of APP. Nature *541*, E1–E2.

Ferretti, M.T., Iulita, M.F., Cavedo, E., Chiesa, P.A., Schumacher Dimech, A., Santuccione Chadha, A., Baracchi, F., Girouard, H., Misoch, S., Giacobini, E., et al.; Women's Brain Project and the Alzheimer Precision Medicine Initiative (2018). Sex differences in Alzheimer disease—the gateway to precision medicine. Nat. Rev. Neurol. *14*, 457–469.

Friedman, B.A., Srinivasan, K., Ayalon, G., Meilandt, W.J., Lin, H., Huntley, M.A., Cao, Y., Lee, S.-H., Haddick, P.C.G., Ngu, H., et al. (2018). Diverse brain myeloid expression profiles reveal distinct microglial activation states and aspects of Alzheimer's disease not evident in mouse models. Cell Rep. *22*, 832–847.

Grabert, K., Michoel, T., Karavolos, M.H., Clohisey, S., Baillie, J.K., Stevens, M.P., Freeman, T.C., Summers, K.M., and McColl, B.W. (2016). Microglial brain region-dependent diversity and selective regional sensitivities to aging. Nat. Neurosci. *19*, 504–516.

Griciuc, A., Serrano-Pozo, A., Parrado, A.R., Lesinski, A.N., Asselin, C.N., Mullin, K., Hooli, B., Choi, S.H., Hyman, B.T., and Tanzi, R.E. (2013). Alzheimer's disease risk gene CD33 inhibits microglial uptake of amyloid beta. Neuron *78*, 631–643.

Guerreiro, R., Wojtas, A., Bras, J., Carrasquillo, M., Rogaeva, E., Majounie, E., Cruchaga, C., Sassi, C., Kauwe, J.S.K., Younkin, S., et al.; Alzheimer Genetic

Analysis Group (2013). TREM2 variants in Alzheimer's disease. N. Engl. J. Med. *368*, 117–127.

Hammond, T.R., Dufort, C., Dissing-Olesen, L., Giera, S., Young, A., Wysoker, A., Walker, A.J., Gergits, F., Segel, M., Nemesh, J., et al. (2019). Single-cell RNA sequencing of microglia throughout the mouse lifespan and in the injured brain reveals complex cell-state changes. Immunity *50*, 253–271.e6.

Harrison, J.R., and Owen, M.J. (2016). Alzheimer's disease: the amyloid hypothesis on trial. Br. J. Psychiatry *208*, 1–3.

Hartl, D., May, P., Gu, W., Mayhaus, M., Pichler, S., Spaniol, C., Glaab, E., Bobbili, D.R., Antony, P., Koegelsberger, S., et al.; AESG (2018). A rare loss-of-function variant of ADAM17 is associated with late-onset familial Alzheimer disease. Mol. Psychiatry, Published online July 9, 2018. https://doi.org/10.1038/s41380-018-0091-8.

Heilmann, S., Drichel, D., Clarimon, J., Fernández, V., Lacour, A., Wagner, H., Thelen, M., Hernández, I., Fortea, J., Alegret, M., et al. (2015). PLD3 in non-familial Alzheimer's disease. Nature *520*, E3–E5.

Herrup, K. (2015). The case for rejecting the amyloid cascade hypothesis. Nat. Neurosci. *18*, 794–799.

Hodes, R.J., and Buckholtz, N. (2016). Accelerating Medicines Partnership: Alzheimer's Disease (AMP-AD) knowledge portal aids Alzheimer's drug discovery through open data sharing. Expert Opin. Ther. Targets *20*, 389–391.

Holtzman, D.M., Bales, K.R., Tenkova, T., Fagan, A.M., Parsadanian, M., Sartorius, L.J., Mackey, B., Olney, J., McKeel, D., Wozniak, D., and Paul, S.M. (2000). Apolipoprotein E isoform-dependent amyloid deposition and neuritic degeneration in a mouse model of Alzheimer's disease. Proc. Natl. Acad. Sci. USA *97*, 2892–2897.

Hooli, B.V., Lill, C.M., Mullin, K., Qiao, D., Lange, C., Bertram, L., and Tanzi, R.E. (2015). PLD3 gene variants and Alzheimer's disease. Nature *520*, E7–E8.

Irizarry, M.C., Cheung, B.S., Rebeck, G.W., Paul, S.M., Bales, K.R., and Hyman, B.T. (2000). Apolipoprotein E affects the amount, form, and anatomical distribution of amyloid beta-peptide deposition in homozygous APP(V717F) transgenic mice. Acta Neuropathol. *100*, 451–458.

Jack, C.R., Jr., Knopman, D.S., Jagust, W.J., Petersen, R.C., Weiner, M.W., Aisen, P.S., Shaw, L.M., Vemuri, P., Wiste, H.J., Weigand, S.D., et al. (2013). Tracking pathophysiological processes in Alzheimer's disease: an updated hypothetical model of dynamic biomarkers. Lancet Neurol. *12*, 207–216.

Karch, C.M., Cruchaga, C., and Goate, A.M. (2014). Alzheimer's disease genetics: from the bench to the clinic. Neuron *83*, 11–26.

Karran, E., and Hardy, J. (2014). A critique of the drug discovery and phase 3 clinical programs targeting the amyloid hypothesis for Alzheimer disease. Ann. Neurol. *76*, 185–205.

Karran, E., Mercken, M., and De Strooper, B. (2011). The amyloid cascade hypothesis for Alzheimer's disease: an appraisal for the development of therapeutics. Nat. Rev. Drug Discov. *10*, 698–712.

Keren-Shaul, H., Spinrad, A., Weiner, A., Matcovitch-Natan, O., Dvir-Szternfeld, R., Ulland, T.K., David, E., Baruch, K., Lara-Astaiso, D., Toth, B., et al. (2017). A unique microglia type associated with restricting development of Alzheimer's disease. Cell *169*, 1276–1290.e17.

Krasemann, S., Madore, C., Cialic, R., Baufeld, C., Calcagno, N., El Fatimy, R., Beckers, L., O'Loughlin, E., Xu, Y., Fanek, Z., et al. (2017). The TREM2-APOE pathway drives the transcriptional phenotype of dysfunctional microglia in neurodegenerative diseases. Immunity *47*, 566–581.e9.

Lambert, J.C., Ibrahim-Verbaas, C.A., Harold, D., Naj, A.C., Sims, R., Bellenguez, C., DeStafano, A.L., Bis, J.C., Beecham, G.W., Grenier-Boley, B., et al.; European Alzheimer's Disease Initiative (EADI); Genetic and Environmental Risk in Alzheimer's Disease; Alzheimer's Disease Genetic Consortium; Cohorts for Heart and Aging Research in Genomic Epidemiology (2013). Meta-analysis of 74,046 individuals identifies 11 new susceptibility loci for Alzheimer's disease. Nat. Genet. *45*, 1452–1458.

Lambert, J.-C., Grenier-Boley, B., Bellenguez, C., Pasquier, F., Campion, D., Dartigues, J.-F., Berr, C., Tzourio, C., and Amouyel, P. (2015). PLD3 and sporadic Alzheimer's disease risk. Nature *520*, E1.

Laws, K.R., Irvine, K., and Gale, T.M. (2018). Sex differences in Alzheimer's disease. Curr. Opin. Psychiatry *31*, 133–139.

Liao, Y., Smyth, G.K., and Shi, W. (2014). featureCounts: an efficient general purpose program for assigning sequence reads to genomic features. Bioinformatics *30*, 923–930.

Makin, S. (2018). The amyloid hypothesis on trial. Nature *559*, S4–S7.

Marioni, R.E., Harris, S.E., Zhang, Q., McRae, A.F., Hagenaars, S.P., Hill, W.D., Davies, G., Ritchie, C.W., Gale, C.R., Starr, J.M., et al. (2018). GWAS on family history of Alzheimer's disease. Transl. Psychiatry *8*, 99.

Masuda, A., Kobayashi, Y., Kogo, N., Saito, T., Saido, T.C., and Itohara, S. (2016). Cognitive deficits in single App knock-in mouse models. Neurobiol. Learn. Mem. *135*, 73–82.

Mathys, H., Adaikkan, C., Gao, F., Young, J.Z., Manet, E., Hemberg, M., De Jager, P.L., Ransohoff, R.M., Regev, A., and Tsai, L.-H. (2017). Temporal tracking of microglia activation in neurodegeneration at single-cell resolution. Cell Rep. *21*, 366–380.

Mazure, C.M., and Swendsen, J. (2016). Sex differences in Alzheimer's disease and other dementias. Lancet Neurol. *15*, 451–452.

Mirra, S.S., Heyman, A., McKeel, D., Sumi, S.M., Crain, B.J., Brownlee, L.M., Vogel, F.S., Hughes, J.P., van Belle, G., and Berg, L. (1991). The Consortium to Establish a Registry for Alzheimer's Disease (CERAD). Part II. Standardization of the neuropathologic assessment of Alzheimer's disease. Neurology *41*, 479–486.

Mootha, V.K., Lindgren, C.M., Eriksson, K.-F., Subramanian, A., Sihag, S., Lehar, J., Puigserver, P., Carlsson, E., Ridderstråle, M., Laurila, E., et al. (2003). PGC-1alpha-responsive genes involved in oxidative phosphorylation are coordinately downregulated in human diabetes. Nat. Genet. *34*, 267–273.

Mostafavi, S., Gaiteri, C., Sullivan, S.E., White, C.C., Tasaki, S., Xu, J., Taga, M., Klein, H.-U., Patrick, E., Komashko, V., et al. (2018). A molecular network of the aging human brain provides insights into the pathology and cognitive decline of Alzheimer's disease. Nat. Neurosci. *21*, 811–819.

Mrdjen, D., Pavlovic, A., Hartmann, F.J., Schreiner, B., Utz, S.G., Leung, B.P., Lelios, I., Heppner, F.L., Kipnis, J., Merkler, D., et al. (2018). High-dimensional single-cell mapping of central nervous system immune cells reveals distinct myeloid subsets in health, aging, and disease. Immunity *48*, 380–395.e6.

Picelli, S., Björklund, Å.K., Faridani, O.R., Sagasser, S., Winberg, G., and Sandberg, R. (2013). Smart-seq2 for sensitive full-length transcriptome profiling in single cells. Nat. Methods *10*, 1096–1098.

Picelli, S., Faridani, O.R., Björklund, A.K., Winberg, G., Sagasser, S., and Sandberg, R. (2014). Full-length RNA-seq from single cells using Smart-seq2. Nat. Protoc *9*, 171–181.

Qiu, X., Mao, Q., Tang, Y., Wang, L., Chawla, R., Pliner, H.A., and Trapnell, C. (2017a). Reversed graph embedding resolves complex single-cell trajectories. Nat. Methods *14*, 979–982.

Qiu, X., Hill, A., Packer, J., Lin, D., Ma, Y.-A., and Trapnell, C. (2017b). Single-cell mRNA quantification and differential analysis with Census. Nat. Methods *14*, 309–315.

Ransohoff, R.M. (2016). A polarizing question: do M1 and M2 microglia exist? Nat. Neurosci. *19*, 987–991.

Rebeck, G.W., Reiter, J.S., Strickland, D.K., and Hyman, B.T. (1993). Apolipoprotein E in sporadic Alzheimer's disease: allelic variation and receptor interactions. Neuron *11*, 575–580.

Rueden, C.T., Schindelin, J., Hiner, M.C., DeZonia, B.E., Walter, A.E., Arena, E.T., and Eliceiri, K.W. (2017). ImageJ2: ImageJ for the next generation of scientific image data. BMC Bioinformatics *18*, 529.

Saito, T., Matsuba, Y., Mihira, N., Takano, J., Nilsson, P., Itohara, S., Iwata, N., and Saido, T.C. (2014). Single App knock-in mouse models of Alzheimer's disease. Nat. Neurosci. *17*, 661–663.

Salih, D.A., Bayram, S., Guelfi, M.S., Reynolds, R.H., Shoai, M., Ryten, M., Brenton, J., Zhang, D., Matarin, M., Botia, J., et al. (2018). Genetic variability in response to Aβ deposition influences Alzheimer's risk. bioRxiv. https://doi.org/10.1101/437657.

Sasaguri, H., Nilsson, P., Hashimoto, S., Nagata, K., Saito, T., De Strooper, B., Hardy, J., Vassar, R., Winblad, B., and Saido, T.C. (2017). APP mouse models for Alzheimer's disease preclinical studies. EMBO J. *36*, 2473–2487.

Schindelin, J., Arganda-Carreras, I., Frise, E., Kaynig, V., Longair, M., Pietzsch, T., Preibisch, S., Rueden, C., Saalfeld, S., Schmid, B., et al. (2012). Fiji: an open-source platform for biological-image analysis. Nat. Methods *9*, 676–682.

Selkoe, D.J., and Hardy, J. (2016). The amyloid hypothesis of Alzheimer's disease at 25 years. EMBO Mol. Med. *8*, 595–608.

Serrano-Pozo, A., Frosch, M.P., Masliah, E., and Hyman, B.T. (2011). Neuropathological alterations in Alzheimer disease. Cold Spring Harb. Perspect. Med. *1*, a006189.

Sims, R., van der Lee, S.J., Naj, A.C., Bellenguez, C., Badarinarayan, N., Jakobsdottir, J., Kunkle, B.W., Boland, A., Raybould, R., Bis, J.C., et al.; ARUK Consortium; GERAD/PERADES, CHARGE, ADGC, EADI (2017). Rare coding variants in PLCG2, ABI3, and TREM2 implicate microglial-mediated innate immunity in Alzheimer's disease. Nat. Genet. *49*, 1373–1384.

Srinivasan, K., Friedman, B.A., Larson, J.L., Lauffer, B.E., Goldstein, L.D., Appling, L.L., Borneo, J., Poon, C., Ho, T., Cai, F., et al. (2016). Untangling the brain's neuroinflammatory and neurodegenerative transcriptional responses. Nat. Commun *7*, 11295.

Subramanian, A., Tamayo, P., Mootha, V.K., Mukherjee, S., Ebert, B.L., Gillette, M.A., Paulovich, A., Pomeroy, S.L., Golub, T.R., Lander, E.S., and Mesirov, J.P. (2005). Gene set enrichment analysis: a knowledge-based approach for interpreting genome-wide expression profiles. Proc. Natl. Acad. Sci. USA *102*, 15545–15550.

Suh, J., Choi, S.H., Romano, D.M., Gannon, M.A., Lesinski, A.N., Kim, D.Y., and Tanzi, R.E. (2013). ADAM10 missense mutations potentiate β-amyloid accumulation by impairing prodomain chaperone function. Neuron *80*, 385–401.

Trapnell, C., Cacchiarelli, D., Grimsby, J., Pokharel, P., Li, S., Morse, M., Lennon, N.J., Livak, K.J., Mikkelsen, T.S., and Rinn, J.L. (2014). The dynamics and regulators of cell fate decisions are revealed by pseudotemporal ordering of single cells. Nat. Biotechnol. *32*, 381–386.

Trombetta, J.J., Gennert, D., Lu, D., Satija, R., Shalek, A.K., and Regev, A. (2014). Preparation of Single-Cell RNA-Seq Libraries for Next Generation Sequencing. Curr. Protoc. Mol. Biol. *107*, 4–22, 1–17.

Ulrich, J.D., Ulland, T.K., Mahan, T.E., Nyström, S., Nilsson, K.P., Song, W.M., Zhou, Y., Reinartz, M., Choi, S., Jiang, H., et al. (2018). ApoE facilitates the microglial response to amyloid plaque pathology. J. Exp. Med. *215*, 1047–1058.

van der Flier, W.M., and Scheltens, P. (2005). Epidemiology and risk factors of dementia. J. Neurol. Neurosurg. Psychiatry *76* (*Suppl 5*), v2–v7.

van der Lee, S.J., Holstege, H., Wong, T.H., Jakobsdottir, J., Bis, J.C., Chouraki, V., van Rooij, J.G.J., Grove, M.L., Smith, A.V., Amin, N., et al. (2015). PLD3 variants in population studies. Nature *520*, E2–E3.

Villa, A., Gelosa, P., Castiglioni, L., Cimino, M., Rizzi, N., Pepe, G., Lolli, F., Marcello, E., Sironi, L., Vegeto, E., and Maggi, A. (2018). Sex-specific features of microglia from adult mice. Cell Rep. *23*, 3501–3511.

Villegas-Llerena, C., Phillips, A., Garcia-Reitboeck, P., Hardy, J., and Pocock, J.M. (2016). Microglial genes regulating neuroinflammation in the progression of Alzheimer's disease. Curr. Opin. Neurobiol. *36*, 74–81.

Wang, M., Beckmann, N.D., Roussos, P., Wang, E., Zhou, X., Wang, Q., Ming, C., Neff, R., Ma, W., Fullard, J.F., et al. (2018). The Mount Sinai cohort of large-scale genomic, transcriptomic and proteomic data in Alzheimer's disease. Sci. Data *5*, 180185.

Yeh, F.L., Wang, Y., Tom, I., Gonzalez, L.C., and Sheng, M. (2016). TREM2 binds to apolipoproteins, including APOE and CLU/APOJ, and thereby facilitates uptake of amyloid-beta by microglia. Neuron *91*, 328–340.

Zhang, B., Gaiteri, C., Bodea, L.-G., Wang, Z., McElwee, J., Podtelezhnikov, A.A., Zhang, C., Xie, T., Tran, L., Dobrin, R., et al. (2013). Integrated systems approach identifies genetic nodes and networks in late-onset Alzheimer's disease. Cell *153*, 707–720.

STAR★METHODS

KEY RESOURCES TABLE

REAGENT or RESOURCE	SOURCE	IDENTIFIER
Antibodies		
anti-CD11b-PE, clone: M1/70.15.11.5	Miltenyi Biotec	130-113-797; RRID: AB_2726320
anti-β-amyloid 1-16 6E10, mouse	BioLegend	803004; RRID: AB_2715854
anti-IBA1, rabbit	Wako-Chemicals	019-19741; RRID: AB_839504
anti-ApoE, goat	Sigma-Aldrich	AB947; RRID: AB_2258475
atto-488-conjugated goat anti-mouse	Sigma-Aldrich	62197-1ML-F; RRID: AB_1137649
Alexa 488 donkey anti-mouse	Invitrogen	A21202; RRID: AB_1137649
Alexa-594 donkey anti-rabbit	Invitrogen	A211207
Alexa-647 donkey anti-goat	Invitrogen	A21447
anti-β-amyloid BAM10, mouse	Sigma-Aldrich	A5213-.2ML; RRID: AB_476742
Alexa-568 goat anti-mouse	Thermo Fisher	A-11004
Chemicals, Peptides, and Recombinant Proteins		
Hibernate A without phenol red	Brain Bits	HAPR
D-PBS	Life Technologies	14287072
MACS BSA stock solution	Miltenyi Biotec	130-091-376
RNasin Plus RNase Inhibitor	Promega	N2615
TrueBlack	Biotium	23007
Critical Commercial Assays		
Adult Brain Dissociation kit	Miltenyi Biotec	130-107-677
Nextera XT kit	Illumina	FC-131-1096
Nextera XT Index Kit v2 Set A (96 indexes, 384 samples)	Illumina	FC-131-2001
Nextera XT Index Kit v2 Set B (96 indexes, 384 samples)	Illumina	FC-131-2002
Nextera XT Index Kit v2 Set C (96 indexes, 384 samples)	Illumina	FC-131-2003
Nextera XT Index Kit v2 Set D (96 indexes, 384 samples)	Illumina	FC-131-2004
RNAscope	ACD	320850
Mm-*Slc1a3* RNAscope probe	ACD	430781
Mm-*Itgam*-C2 RNAscope probe	ACD	311491-C2
Mm-*Apoe*-C3 RNAscope probe	ACD	313271-C3
Deposited Data		
Raw data	This paper	GEO: GSE127893
Analyzed data	This paper	scope.bdslab.org
Human RNaseq data (AMP-AD)	Allen et al., 2016	MSBB synapse ID: syn3157743 ROSMAP synapse ID: syn3388564
Experimental Models: Organisms/Strains		
App^{NL-G-F}	Saito et al., 2014	Available from the Saido lab.
C57BL/6J (control for *App*$^{NL-G-F}$)	Janvier	C57BL/6J@Rj
APPswe/PS1dE9 (*APP/PS1*)	Borchelt et al., 1997	Available from The Jackson Laboratory, stock 34829-JAX
APP/PS1-Apoe^{null}	Hudry et al., *in preparation*	Available from the Hyman lab.
C57BL/6J	The Jackson Laboratory	000664
C57BL/6J-Apoe^{null}	The Jackson Laboratory	002052

(Continued on next page)

Continued

REAGENT or RESOURCE	SOURCE	IDENTIFIER
Oligonucleotides		
5′-biotinylated template switching oligo: /5Biosg/ AAGCAGTGGTATCAACGCAGAGTACATrGrG+G	this paper	Exiqon/QIAGEN
5′-biotinylated oligo-dT: /5Biosg/AAGCAGTGGTAT CAACGCAGAGTACTTTTTTTTTTTTTTTTTTTTTTTTT TTTTTTVN	Picelli et al., 2013	IDT
5′-biotinylated IS-PCR oligo: /5Biosg/AAGCAGT GGTATCAACGCAGAGT	Picelli et al., 2013	IDT
Software and Algorithms		
STAR RNA-seq aligner, v. 2.5.2	Dobin et al., 2013	https://github.com/alexdobin/STAR
Subread/Featurecounts, v. 1.5.1	Liao et al., 2014	http://subread.sourceforge.net/
R, v. 3.4.4	R core team	https://www.R-project.org/
Seurat, v. 2.3.1	Butler et al., 2018	https://github.com/satijalab/seurat
Monocle, v. 2.6.4	Qiu et al., 2017a	https://github.com/cole-trapnell-lab/monocle-release
Fiji	Schindelin et al., 2012	https://fiji.sc/

CONTACT FOR REAGENT AND RESOURCE SHARING

Further information and requests for resources and reagents should be directed to and will be fulfilled by the Lead Contact, Prof. Bart De Strooper (bart.destrooper@kuleuven.vib.be).

EXPERIMENTAL MODELS DETAILS

Mice

For the 3, 6 and 12 m.o. time points we used homozygous App^{NL-G-F} (Saito et al., 2014) mice, backcrossed for at least 2 generations with *C57BL/6J* mice in the De Strooper lab, and wild-type *C57BL/6J* mice themselves. For the 21 m.o. time point, both App^{NL-G-F} and *C57BL/6J* mice were transferred from the Saido lab to the De Strooper lab, and housed at least 1 month before being used for experiments. Both male and female App^{NL-G-F} and *C57BL/6J* mice were used for experiments. The novel $APP/PS1-Apoe^{null}$ strain is described in another manuscript [Hudry et al., submitted]. Briefly, *APPswe/PS1dE9* (*APP/PS1*) were crossed with a *C57BL/6J-Apoe^{null}* breeder to obtain homozygous $APP/PS1-Apoe^{null}$ mice. $APP/PS1-Apoe^{null}$ mice, along with parental *APP/PS1* mice and the respective control strains *C57BL/6J* and $C57BL/6J-Apoe^{null}$, were transferred from the Hyman lab to the De Strooper lab, and housed for at least 1 month before being used for experiments. Only male *APP/PS1*, $APP/PS1-Apoe^{null}$, *C57BL/6J* and $C57BL/6J-Apoe^{null}$ were used. In every case, mice were housed according to the appropriate institution's ethical requirements, and in compliance to the country's laws for animal research.

METHOD DETAILS

Single cell suspension preparation

Mice were euthanized with CO_2 and then rapidly perfused with ice cold PBS for 10-15 minutes using a pumping rate of 100 mL/h. The dissection (Srinivasan et al., 2016) and microglia isolation steps were carried out on ice or at +4°C, to minimize microglia activation due to technical artifacts. We removed the brain and placed it on a chilled glass plate sitting on wet ice. We quickly dissected the whole cortex and the whole hippocampus separately, using instruments chilled on ice. The tissue was finely chopped using a chilled razorblade and then transferred to a tube containing ice-cold Hibernate A medium without phenol red (BrainBits, Springfield, IL). For each experimental condition we pooled tissue from two mice. We prepared a single cell suspension from the minced tissue using the Adult Brain Dissociation kit from Miltenyi Biotec (Bergisch Gladbach, Germany) adapting manufacturer's recommendations for manual tissue processing. First, we pelleted the tissue chunks by centrifugation (300 g for 2 minutes at 4°C), removed the Hibernate A medium and resuspended the tissue in a mix of buffer Z with enzymes P, A and Y prepared according to the manufacturer's instructions. We next placed the tubes horizontally on ice for 30 minutes, with mechanical dissociation steps performed at 10 minutes intervals (first with 5 mL pipettes, then with fire-polished glass Pasteur pipettes, and lastly with P1000 tips). The resulting cell suspension was filtered on a 70 μm cell strainer, and the strainer was washed with 10 mL of D-PBS containing magnesium, calcium, glucose, and pyruvate (Life Technologies, Carlsbad, CA). Cells were centrifuged, resuspended in D-PBS, gently mixed with Debris Removal Solution, and overlaid with D-PBS according to manufacturer's instructions. After centrifugation (3000 g for 10 minutes at

4°C), cells were washed once with D-PBS, resuspended in 1X Red Blood Cell Removal Solution, incubated for 10 minutes at 4°C, diluted 10 times with D-PBS containing 0.5% BSA (Miltenyi Biotec), and pelleted by centrifugation. Cells were finally resuspended in D-PBS containing 0.5% BSA.

Single microglia isolation by FACS

The single cell suspension was stained by incubation for 20 minutes on ice with anti-CD11b-PE conjugated primary antibody (Miltenyi Biotec) at a 1:10 dilution. Just before loading on the sorter, cells were stained with DAPI (1:5000 final dilution). Cell sorting was performed with a BD FACSAria III (BD Biosciences, Franklin Lakes, NJ). Gating was calibrated by running non-stained and single stained (anti-CD11b-PE only and DAPI-only) samples. Single live microglia cells (CD11b+/DAPI-) were sorted into independent wells of a 96-well plate, preloaded with 4 μL of 0.2% Triton in Ultrapure water (GIBCO), containing 1 U/μL of RNasinPlus RNase inhibitor (Promega, Madison, WI). After sorting, plates were sealed, briefly centrifuged, snap frozen on dry ice, and stored at −80°C until further processing.

Single cell mRNA libraries preparation and sequencing

Single cell retrotranscription and preparation of sequencing libraries was performed using a modified SmartSeq2 protocol (Picelli et al., 2013, 2014; Trombetta et al., 2014) to improve the yield of cDNA from single microglia cells. We used 5′-biotinylated primers throughout the protocol, oligo-dT and IS-PCR oligos were obtained from Integrated DNA Technologies (Skokie, IL), while template-switching oligo (TSO) was from Exiqon (Vedbaek, Denmark). First, 96-well plates with single sorted cells were thawed on ice, and we added to each well 1 μL of 10 mM dNTPs, 0.5 μL of 5 μM oligo-dT, and 0.5 μL of a 1:2660000 dilution of ERCC RNA Spike-In mix (ThermoFisher, Waltham, MA). After incubating the plate at 72°C for 3 minutes, we added to each well a retrotranscription mix (containing 1.5X First Strand buffer, 6.1 mM DTT, 1.7 M betaine, 10 mM MgCl2, 0.6 U/μL SUPERase IN, 11.1 U/μL SuperScript II polymerase, and 1.3 μM TSO oligo). All retrotranscription mix components were from the SuperScript II Reverse Transcriptase kit (ThermoFisher), except betaine (Sigma, St. Louis, MO), SUPERase IN (ThermoFisher), and the TSO oligo. Retrotranscription reaction was carried out for 90 minutes at 42°C, followed by 10 cycles of 2 minutes at 50°C and 2 minutes at 42°C, and completed by a 15 minutes incubation at 70°C. Next, we added to each well a preamplification mix containing 1X Kapa HiFi HS readymix (Kapa Biosystems, Wilmington, MA) and 0.2 μM of IS-PCR primer. Preamplification was carried out for 23 cycles (98°C for 20 s, 67°C for 15 s, 72°C for 6 minutes). PCR products were purified using AMPure XP beads (Beckman Coulter, Brea, CA) at 1:0.6 ratio and according to manufacturer's recommendations and eluted in 12 μL of EB buffer (QIAGEN, Hilden, Germany). cDNA preparation was checked by analyzing several random wells for each plate on an Agilent BioAnalyser DNA High Sensitivity chip (Agilent, Santa Clara, CA). We used the Nextera XT kit (Illumina, San Diego, CA) to tagment 1.25 μL of 1:15 diluted cDNA per reaction. Tagmentation reactions were assembled at room temperature (RT) using 2.5 μL of TD buffer and 1.25 μL of ATM mix per sample, incubated at 55°C for 8 minutes, and then immediately placed on hold at 10°C. We next added 1.25 μL of NT buffer (Illumina) and further incubated for 5 minutes at RT. To amplify tagmentation products, we added 1.25 μL of appropriate indexed forward and reverse primers (Nextera XT Index kit v2, sets A, B, C, or D, all from Illumina), and 3.75 μL of NPM mix (Illumina). Amplification reaction was carried out for 12 cycles (95°C for 10 s, 55°C for 30 s, 72°C for 30 s). Amplified products from each 96 well plate were pooled and purified using AMPure XP beads at 1:0.7 ratio. Purified pools were checked on an Agilent BioAnalyser DNA High Sensitivity chip, and quantified by quantitative PCR using the Kapa Library Quantification kit for Illumina libraries. Four 96-well plate pools with compatible indexes were further pooled to yield 384-samples libraries. Each library was sequenced on an Illumina NextSeq550 system using single end 75 base pair sequencing kits (Illumina).

Sequencing data analysis

Demultiplexed FASTQ files were aligned to the mouse genome (mm10 build) using STAR version 2.5.2 (Dobin et al., 2013) with default options. Reads aligned to each gene were counted using featureCounts version 1.5.1 (Liao et al., 2014) with options -g gene_name -Q 10. The count table was imported in R (version 3.4.4) for analysis. Data generated from App^{NL-G-F} and $C57BL/6J$ mice, and data generated from $APP/PS1$, $APP/PS1-Apoe^{null}$, $C57BL/6J$ and $C57BL/6J-Apoe^{null}$ mice are referred here as two separate datasets.

Quality control of cells - step 1

For each dataset, to exclude poorly sequenced cells, damaged cells and dying cells, we filtered out cells outside the limits of median ± 4 * median absolute deviations for both reads number and genes detected; moreover, we excluded cells with more than 10% of reads aligning to mitochondrial genes (Figure S2A and Figure S6A). Data was analyzed by principal component analysis (PCA) to identify obvious batch effects, in which case we would discard the entire 96-well plate (we excluded two plates following this procedure). For the first dataset, the median depth of sequencing was 572,294 reads/cell, with an interquantile range of 253,445 reads/cell, while the median number of genes detected per cell was 2,250 (interquantile range: 572). After quality control (Figure S2A) we retained 11,038 cells for further analysis, with at least 270 cells for each experimental condition (Table S1).

Quality control of cells - step 2

For each dataset, we applied a workflow based on the R package Seurat (version 2.3.1 (Butler et al., 2018)) to identify and remove non-microglia cells before proceeding with analysis. For the first dataset, after data normalization and scaling, we performed principal component analysis (PCA) on the 4,687 most variable genes detected. Based on a scree plot (i.e., a plot of the PC eigenvalues in decreasing order) of standard deviations of the principal components (PCs), we selected the first 17 PCs as input for the

calculations to identify cell clusters (Seurat *FindClusters* function). We then performed non-linear dimensionality reduction and we visualized cell clusters on a t-SNE plot (Figure S3A). We identified 10 major cellular populations, most of them showing a tight distribution on the t-SNE plot, with only two clusters (7 and 9) clearly separating (Figure S2B). Based on a panel of marker genes (Figure S2C), we had no enrichment for markers of brain cells other than microglia, but two clusters (7 and 9, figure S2B-C) showed high expression levels of genes markers of perivascular macrophages (*Mrc1*) and neutrophils (*Ccr2* and *Pldb1*). Indeed, clusters 7 and 9 scored low for a microglial genes signature (Figure S2D) and high for a neutrophil genes signature (Figure S2E). We did not find cells expressing gene signatures of other brain cells (Figure S2C: neurons (*Gria2*), astrocytes (*Aqp4*), oligodendrocytes (*Olig1*)), confirming that 97.9% of cells (10,801/11,038) in our post-QC dataset were microglia. Only the 10,801 microglia cells were retained for further analysis. For the second dataset, we considered the top 4,711 most variable genes, and we used the first 12 PCs for initial clustering. We identified several clusters, with one displaying high score for a neutrophil marker genes signature (cluster 12, Figure S6E), which was removed prior to subsequent analysis. The other cells scored high for a microglia marker genes signatures (Figure S6D), while expression of markers of other brain cell types were low or null (Figure S6C).

Clustering
Cells passing QC were analyzed using functions provided with the Seurat package. Data was log normalized and we regressed out the variables of read count and percentage of reads aligning on mitochondrial genes. Next, we identified the genes with highest variability and performed PCA on such gene set. We identified the most informative principal components based on a scree plot and we used these to perform cell clustering. Identification of differential expressed genes was performed using the Wilcox test implemented by Seurat's *FindMarker*. t-SNE plots were prepared using Seurat's t-SNE implementation. For the first dataset, we considered 4,777 highly variable genes for PCA and the first 14 PCs for clustering. The second dataset was analyzed similarly as described above, by performing PCA on the 4,967 most variable genes and by using the first 10 PCs to perform cluster analysis.

Pseudotime analysis
To infer the pseudotime of microglia progression toward response development we used functions provided with the Monocle 2 package (version 2.6.4 (Qiu et al., 2017a, 2017b; Trapnell et al., 2014)). We performed a semi-supervised identification of cell trajectories and states, based on marker genes identified during clustering. Briefly, we defined a series of genes (*Apoe*, *Ifit3*, *H2-Aa*, *Dkk2*), which are selectively expressed in each response type (main response and interferon-based) and in the subpopulations identified, which we used to build a classifier (*CellTypeHierarchy*) to assign cell identities in terms of microglia states of activation. We then calculated a covariance matrix for these marker genes, and we used the top 1000 genes (ranked by *p value adjusted*) to calculate single cell trajectories.

Differential Expression
Differential expression was performed using functions provided with the Seurat package; p values were calculated using the Wilcoxon rank-sum test, with all Seurat parameters set to default. Genes with adjusted p values (using a Bonferroni correction) < 0.05, and ln fold changes > |0.2| were considered significantly differentially expressed.

Z scores of microglia responses signatures
For Figure 3, signatures were calculated using Seurat's *AddModuleScore* function using a list of relevant genes identified from GSEA as input. For Figure 5, Z scores were calculated by considering the top genes showing differential expression between ARM and homeostatic cells in the App^{NL-G-F} dataset (n genes = 18) or between the IRM and homeostatic cells in the App^{NL-G-F} dataset (n genes = 28), respectively. Top genes were defined as being statistically significant after multiple testing correction and displaying at least 1 ln fold change. *Apoe* was excluded from the gene signature to avoid skewing the calculations in $Apoe^{null}$ samples.

Human RNaseq data analysis
We analyzed RNaseq data obtained from the AMP-AD (Accelerating Medicines Partnership – Alzheimer's disease) portal (Hodes and Buckholtz, 2016) for the ROSMAP (Religious Orders Study and Memory and Aging Project) (Mostafavi et al., 2018) and MSBB (Mount Sinai Brain Bank) cohorts (Wang et al., 2018). The identifiers for these studies on the AMP-AD portal (www.synapse.org) are syn3157743 for MSBB and syn3388564 for ROSMAP. The reads were trimmed, aligned and mapped to the reference genome and the transcript expression levels quantified by their automated pipelines. The ROSMAP study provides RNaseq data from the Dorsolateral Prefrontal Cortex and the MSBB study has samples from the Prefrontal Cortex (PFC), Inferior Frontal Gyrus (IFG), Superior Temporal Gyrus (STG) and Parahippocampal Gyrus (PHG). Genes were considered to be microglial of their expression was at least two times the average expression in other cell types, according to cell type specific data provided by the "brain RNA seq" web portal (https://web.stanford.edu/group/barres_lab/brain_rnaseq.html). Sequencing data was analyzed as described in Bihlmeyer et al. (2019), and differential expression analysis was conducted using CERAD staging (Mirra et al., 1991) between C3 and C0 subjects.

Multiplex RNAscope and immunofluorescence staining
Mice were euthanized with CO_2 and then rapidly perfused with ice cold PBS (10 minutes at 100 mL/h). Brain was removed and separated into two hemispheres. One hemisphere was then embedded in molds containing Tissue-Tek OCT (VWR, Radnor, PA), snap frozen in a bath of ethanol and dry ice, and stored at $-80°C$ to perform RNAscope experiments, while the other hemisphere was processed for immunostaining as described below.

OCT-embedded hemispheres were cut into 14 μm sagittal sections using a CryoStar NX70 cryostat (ThermoFisher), layered on SuperFrost Plus glass slides (ThermoFisher) and further stored at −80°C before proceeding with experiments.

RNAscope experiments were performed using the Manual Fluorescent Multiplex kit v1 (Advanced Cell Diagnostics, Newark, CA) following manufacturer's recommendations with minor adjustments. After fixation in 4% paraformaldehyde (PFA) for 30 minutes, sections were dehydrated using a series of ethanol dilution steps; protease digestion was performed for 20 min at RT using Protease IV for fresh frozen tissue provided in the kit, and probes hybridization was carried out for 2 hours at 40°C. We used the following probe sets (all from Advanced Cell Diagnostics): Mm-*Slc1a3* (430781), Mm-*Itgam*-C2 (311491-C2), Mm-*Apoe*-C3 (313271-C3). Immediately after the RNAscope amplification steps, the sections were rinsed briefly with PBS and blocked for 1 hour at RT in PBS containing 0.3% Triton X-100 and 5% normal goat serum. Sections were then immunostained with the anti-β-amyloid 1-16 6E10 primary antibody (BioLegend, San Diego, CA) at 4°C overnight, washed 3 times for 5 minutes in PBS, and further stained for 1 hour at RT with an Atto-488-conjugated goat anti-mouse secondary antibody (Sigma-Aldrich, Saint Louis, MO). Sections were then incubated for 30 s in a 1X TrueBlack (Biotium, Fremont, CA) solution to reduce lipofuscin autofluorescence, washed briefly and stained with DAPI (Sigma-Aldrich). Sections were mounted with FluorSave Reagent (Merck Millipore, Burlington, MA). Imaging was carried out on a Leica TCS SP8 X confocal microscope (Leica Microsystems, Wetzlar, Germany) using a 40X objective, images were analyzed using Fiji ImageJ (Rueden et al., 2017; Schindelin et al., 2012).

RNAscope image analysis and quantification

Three 21-25 months old mice for each *C57BL/6J* and *App^{NL-G-F}* strain were used for the quantifications. For each mouse, four images of the hippocampus (two of CA1, one of CA2 and one of CA3) and five images throughout the isocortex were acquired and stacked in Fiji ImageJ. NIS-elements software (Nikon, Amsterdam, Netherlands) was used to detect nuclei, microglia, astrocytes and plaques using a custom-made protocol. Nuclei and cell body perimeter were established using the DAPI signal; microglia and astrocytes were identified by RNAscope puncta from the *Itgam* and *Slc3a1* probes. All parameters were kept constant between images to allow unbiased detection. Plaque staining was judged individually in each image, as plaques vary greatly in size and intensity of staining. Arbitrary plaques were drawn in the images of *C57BL/6J* mice. Images from *C57BL/6J* and *App^{NL-G-F}* mice were analyzed in the same manner, for the latter mice we considered only the dense plaques. Around each plaque, five concentric circles of 18.2 μm were drawn, for each circle we counted microglia and astrocytes cells, and for each cell we measured the intensity of the signal from the *Apoe* probeset.

Immunofluorescence staining

Mice were sacrificed with CO_2 and perfused with ice cold PBS (10 minutes at 100 mL/h), and the brain divided into two hemispheres as described above. One of the hemispheres was fixed in 4% PFA overnight and then stored in PBS containing 0.01% sodium azide at +4°C until sectioning on a vibratome. For sectioning, the hemispheres were embedded in UltraPure agarose (Invitrogen, Carlsbad, CA) and cut into 35 μm sections on a Vibratome Leica VT1000S. Antigen retrieval was performed using boiling citrate buffer (Sigma-Aldrich) at pH 6.0. The sections were then blocked in PBS with 0.3% Triton X-100 and 5% normal donkey serum for 1h at RT and incubated in primary antibody at 4°C overnight. The following day sections were washed with PBS and incubated with secondary antibodies for 1 hour at RT. Nuclei were stained with DAPI and sections were mounted with Fluorosave (Merck Millipore). The following primary antibodies were used: mouse anti-β-amyloid 1-16 6E10 (BioLegend), rabbit anti-Iba1 (Wako-Chemicals, Neuss, Germany), goat anti-ApoE (Sigma-Aldrich). Secondary antibodies were: donkey anti-mouse Alexa 488 (Invitrogen A21202), donkey anti-rabbit Alexa 594 (Invitrogen A211207), donkey anti-goat Alexa 647 (Invitrogen A21447).

Amyloid load analysis

Tissue collection and processing

Mice were euthanized by CO_2 asphyxiation and the brain tissue collected for immunohistochemical analysis. After fixation in 4% paraformaldehyde and cryoprotection in 30% glycerol, 40 μm-thick floating sections were cut on a freezing microtome. Floating sections were permeabilized in 0.5% triton in TBS, blocked in 5% normal goat serum in TBS, and incubated with primary antibody (mouse anti-amyloid β Bam10, Sigma-Aldrich; rabbit anti-Iba-1, Wako) overnight at 4°C. Sections were then incubated with appropriate Alexa Fluor 488 or Alexa Fluor 568 conjugated secondary antibodies. Sections were mounted onto slides and coverslipped with Vectashield mounting medium with DAPI (Vector Labs, Burlingame, CA). For the counterstaining of dense-core amyloid plaques, the floating sections were incubated for 15 minutes in a solution of 1 μg/ml of Methoxy-XO4 (diluted in TBS) before mounting the slices with Fluoromount-G (No DAPI, SouthernBiotech, Birmingham, AL).

Stereology-based quantitative analyses

For the quantification of amyloid load, Alexa-568-anti-Amyloid immunolabeled and Methoxy-XO4 positive plaques were imaged using a NanoZoomer-XR Digital slide scanner (Hamamatsu Photonics, Shizuoka, Japan) under a 20X objective. The total surface of amyloid was determined using a custom-written script based on the "*Analyze particle*" function of Fiji (National Institutes of Health: http://fiji.sc/), after defining the cortex as region of interest. The total surface occupied by amyloid was then reported to the cortical area of each section considered. Stereology-based study of amyloid-associated microglia was performed on immunolabeled sections using an Olympus BX52 epifluorescent microscope equipped with motorized stage, DP70 digital CCD camera, and CAST stereology software (Olympus, Tokyo, Japan). The cortex was outlined and microglia counts were made using 20X high

numerical aperture (1.2) objective. Using a meander sampling of 70% of cortical area, images were captured each time an amyloid deposit was encountered. Those images were then analyzed using Fiji, counting the number of Iba1-positive microglial cells close to a plaque (< 50 μm) and reporting this number to the surface of the plaque considered. All pathology quantification was carried out blinded until the last statistical analyses.

QUANTIFICATION AND STATISTICAL ANALYSIS

Statistical details of experiments can be found in the respective figure legends and method sections. We provide here a brief summary.

Differential gene expression
Differential expression was performed using functions provided with the Seurat R package. To calculate p values, we used the Wilcoxon rank-sum test with default parameters, and we used a Bonferroni correction to calculate adjusted p values for multiple testing. Genes with adjusted p values < 0.05, and with a fold change (ln scale) > |0.2| were considered significantly differentially expressed.

RNAscope signal quantification and cell count
Around each plaque, or an arbitrary point in C57BL/6J mice, we drew five concentric circles of 18.2 μm. We counted microglia (*Itgam+*) and astrocytes (*Slc1a3+*) in each ring, and for each cell we measured the intensity of the signal from the *Apoe* probeset using the Fiji software.

Stereological quantification of amyloid burden and microglia density
Sections were imaged with a 20X objective and an epifluorescent microscope, and data were analyzed using a custom script based on the "*Analyze particle*" function of Fiji software. 5 to 7 mice per group werer analyzed, p values were calculated using the Mann-Whitney test.

DATA AND SOFTWARE AVAILABILITY

Raw and normalized gene expression data have been deposited in GEO (GEO: GSE127893). Data can be browsed interactively at: scope.bdslab.org